

DIAMOND-SSS: Diffusion-Augmented Multi-View Optimization for Data-efficient SubSurface Scattering

Guillermo Figueroa-Araneda*
 Technical University of Munich
 guillermo.figueroaa@usm.cl

Florian Hofherr
 Technical University of Munich
 florian.hofherr@tum.de

Manny Ko
 Independent Researcher
 man961@yahoo.com

Daniel Cremers
 Technical University of Munich
 cremers@tum.de

Iris Diana Jimenez*
 Ludwig-Maximilians-Universität Munich
 jimenez@lmu.de

Hector Andrade-Loarca
 Technical University of Munich
 hector.andrade@tum.de

Abstract

Subsurface scattering (SSS) gives translucent materials—such as wax, jade, marble, and skin—their characteristic soft shadows, color bleeding, and diffuse glow. Modeling these effects in neural rendering remains challenging due to complex light transport and the need for densely captured multi-view, multi-light datasets (often > 100 views and 112 OLATs).

We present **DIAMOND-SSS**, a data-efficient framework for high-fidelity translucent reconstruction from extremely sparse supervision—even as few as ten images. We fine-tune diffusion models for novel-view synthesis and relighting, conditioned on estimated geometry and trained on less than 7% of the dataset, producing photorealistic augmentations that can replace up to 95% of missing captures. To stabilize reconstruction under sparse or synthetic supervision, we introduce illumination-independent geometric priors: a multi-view silhouette consistency loss and a multi-view depth consistency loss. Across all sparsity regimes, **DIAMOND-SSS** achieves state-of-the-art quality in relightable Gaussian rendering, reducing real capture requirements by up to 90% compared to SSS-3DGS.

1. Introduction

Rendering translucent materials such as skin, wax, or jade remains challenging in graphics and vision. Their appearance is governed by *subsurface scattering* (SSS)—light entering a surface, scattering within the medium, and exiting else-

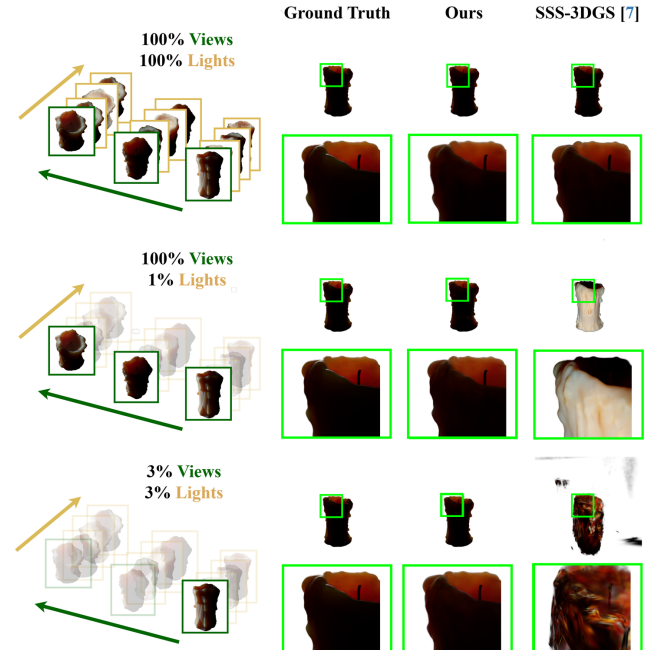


Figure 1. We propose a data-efficient framework for re-lightable 3D with subsurface scattering. Unlike prior work [7] requiring **many viewpoints under multiple illuminations**, our method uses diffusion models to synthesize novel views and lighting from sparse observations. The baseline [7] massively overfits in the second row, for the only given light condition.

where—producing soft glows, color bleeding, and blurred shadows. Accurately capturing these effects requires jointly modeling geometry, illumination, and volumetric transport,

*Equal contribution.

making data acquisition costly and dependent on dense, controlled multi-view and multi-light setups.

Neural rendering methods such as NeRF [21] and 3D Gaussian Splatting (3DGS) [17] enable high-quality novel-view synthesis, but entangle lighting and appearance, limiting relighting. Physically based extensions incorporate BRDF models [4, 5, 22] under known [2, 3, 30, 39] or unknown [1, 9, 15, 37, 38] illumination, or account for indirect lighting [25, 43, 44]. While effective for opaque materials, these methods cannot reproduce the spatially decoupled transport characteristic of translucent media.

Modeling SSS requires volumetric light transport. Classical BSSRDF (Bidirectional Scattering Surface Reflectance Distribution Function) models [6, 8, 12, 13] offer analytic approximations but struggle with real-world complexity. Learning-based SSS methods [18, 31, 32, 46] provide more flexibility but still require dense, calibrated data.

KiloOSF [36] learns object-centric scattering functions yet remains surface-bound. The current state of the art, SSS-3DGS [7], augments Relightable 3DGS [9] with a residual MLP to capture volumetric scattering, achieving photorealistic translucency—but at the cost of dense supervision: over 100 calibrated views and 112 OLAT illuminations per object.

Our approach. We present **DIAMOND-SSS**, a data-efficient extension of SSS-3DGS [7] for relightable reconstruction of translucent materials from sparse supervision. While SSS-3DGS requires tens of thousands of images across ~ 100 views and 112 OLAT illuminations, DIAMOND-SSS attains comparable or superior quality using as little as ten views and one light.

Our key component is a *diffusion-based augmentation pipeline* that synthesizes missing viewpoints and lighting via two geometry-conditioned diffusion models—one for novel-view generation and one for relighting—fine-tuned on less than 7% of the dataset yet producing photorealistic, geometrically aligned augmentations. To stabilize reconstruction under sparse or synthetic data, we introduce two illumination-invariant geometric priors: multi-view silhouette consistency and multi-view depth consistency, which regularize structure across viewpoints and complement diffusion-based augmentation.

Across all supervision regimes, DIAMOND-SSS surpasses prior work. Geometric priors alone improve fidelity, and combined with diffusion-based relighting enable high-quality reconstructions with up to 95% fewer real captures. Even under extreme sparsity (3% views, 3% lights), our method faithfully reproduces subsurface scattering effects—unattainable with previous approaches.

Contributions.

- We introduce a *diffusion-based augmentation pipeline* for subsurface scattering reconstruction, with fine-tuned models for novel-view synthesis and relighting synthesis of

translucent objects. This enables photometrically and geometrically consistent supervision even under extremely sparse captures (Secs. 3.2 and 3.4).

- We design two *multi-view geometric consistency losses*—silhouette and depth—that complement diffusion-based data augmentation by enforcing structural alignment across viewpoints and improving stability under limited or synthetic supervision (Sec. 3.3).
- We demonstrate that by combining our diffusion-based data augmentation with geometric consistency losses, DIAMOND-SSS achieves high-quality translucent reconstructions with up to **90% less real data** than prior SSS-3DGS approaches, while maintaining fidelity across varying sparsity regimes (Sec. 4).

2. Related Work

2.1. Neural Rendering and Physically-Based Relighting

Neural Radiance Fields (NeRF) [21] and 3D Gaussian Splatting (3DGS) [17] have established high-quality novel-view synthesis by combining scene representation as radiance fields with volumetric rendering. While they show impressive results they entangle appearance and illumination and effectively bake a static lighting into the scene representation, which does not allow for relighting.

To address this limitation large body of work extends these methods with physically based reflectance modeling. Approaches integrate microfacet [5] or Disney BRDFs [4] under known [2, 3, 30, 39] or unknown [1, 9, 15, 37, 38] lighting conditions, or incorporate indirect illumination [44] and more general appearance decompositions [25, 43]. These methods achieve relightable reconstructions but remain focused on opaque materials where light transport is surface-bounded.

2.2. Subsurface Scattering Models

Subsurface scattering (SSS) describes light entering a surface, scattering within a medium, and exiting elsewhere. Classical BSSRDF models—dipole [13], multipole [12], spectral/multilayer skin models [8], and quantized diffusion [6]—are efficient but rely on strong assumptions that limit realism.

Learning-based alternatives, including Neural SSS [32], Li *et al.* [18], Zhu *et al.* [46], and TG *et al.* [31], relax these assumptions but still require dense multi-view, multi-light supervision. KiloOSF [36] introduces object-centric scattering functions but remains surface-bound, while SSS-3DGS [7] models volumetric SSS via a residual MLP atop Gaussian splats, still demanding dense captures. Our method leverages diffusion-based synthetic augmentation and illumination-invariant geometric priors to achieve comparable or superior quality with up to **90% less real data**.

2.3. Diffusion Models for Novel View Synthesis and Relighting

Diffusion models have recently advanced novel view synthesis (NVS). Single-view methods such as Zero-1-to-3 [19] generate pose-controlled views from one RGB input, while multi-view-consistent models including SyncDreamer [20], MVDream [28], Free3D [45], and Cat3D [10] produce coherent view sets and can augment sparse observations for 3D reconstruction. Controllable diffusion frameworks like ControlNet [40] enable conditioning on geometric cues, and Poirier-Ginter *et al.* [23] use such conditioning for OLAT-based relighting via lighting-direction controls.

Building on these advances, our augmentation pipeline (Sec. 3.2) employs two geometry-conditioned diffusion models—one for novel-view synthesis and one for relighting—fine-tuned on a small subset of translucent objects. Integrated into our reconstruction framework (Sec. 3.4), these models produce photometrically and geometrically aligned augmentations. To our knowledge, DIAMOND-SSS is the first to combine diffusion-based augmentation with Gaussian Splatting for data-efficient translucent reconstruction.

2.4. Geometric Supervision under Sparse and Synthetic Settings

Cross-view geometric constraints provide strong cues for 3D reconstruction, particularly under sparse or inconsistent photometric supervision. Silhouette consistency, used since early visual hull methods, has been applied to neural fields [18] to improve shape regularity, while multi-view depth consistency enforces alignment across illuminations.

In our framework (Sec. 3.3), we extend these ideas with illumination-invariant multi-view silhouette and depth consistency losses that stabilize optimization when real data are limited or synthetic supervision is used. Together with our diffusion-based augmentation (Sec. 3.2), these geometric priors form the foundation of DIAMOND-SSS’s data efficiency and reconstruction fidelity.

3. Method

We build on Subsurface Scattering Gaussian Splatting (SSS-3DGS) [7], which extends 3D Gaussian Splatting (3DGS) [17] to represent translucent materials. Our method improves data efficiency through two main contributions: (i) a diffusion-based data augmentation strategy for generating novel views and relighting, and (ii) multi-view geometric consistency losses that enhance reconstruction fidelity under sparse captures.

3.1. Recap: SSS-3DGS

Vanilla 3DGS. 3D Gaussian Splatting represents a scene as a set of N anisotropic Gaussians:

$$G = \{(\mu_i, \Sigma_i, c_i, o_i)\}_{i=1}^N,$$

where $\mu_i \in \mathbb{R}^3$ is the mean position, $\Sigma_i \in \mathbb{R}^{3 \times 3}$ is the covariance matrix defining scale and orientation, c_i is the color, and $o_i \in [0, 1]$ is the opacity. The covariance matrix is parameterized via Cholesky decomposition to ensure positive semi-definiteness, and eigenvalue clamping constrains the spatial extent.

Extended Shading with BRDF and SSS. To model standard surface appearance in Gaussian splatting, each Gaussian is typically augmented with physically motivated material attributes $c_i \in [0, 1]^3$ (albedo), $r_i \in [0, 1]$ (roughness), and $m_i \in [0, 1]$ (metalness) [9]. Shading is then computed in a deferred pass using a microfacet BRDF:

$$C_{\text{surf}}(x) = C_{\text{surf}}(x; c, r, m, \mathbf{n}, \ell), \quad (3.1)$$

where \mathbf{n} is the surface normal, and ℓ the light direction. Dihlmann et al. [7] extend this formulation to handle translucent materials by introducing an additive neural residual term that models subsurface scattering. The final pixel intensity becomes

$$I(x) = C_{\text{surf}}(x) + C_{\text{sss}}(x; \ell, \mathbf{v}, \phi), \quad (3.2)$$

where \mathbf{v} is the view direction and ϕ denotes learned latent features capturing material-dependent scattering behavior.

Surface Shading. Under OLAT lighting with directional source ℓ and radiance $L(\ell)$, surface shading is given by:

$$C_{\text{surf}} = L(\ell) \cdot f_r(\mathbf{n}, \mathbf{v}, \ell; c, r, m) \cdot \max(0, \mathbf{n} \cdot \ell), \quad (3.3)$$

where the BRDF is composed of diffuse and specular components:

$$f_r = f_{\text{diff}} + f_{\text{spec}},$$

$$f_{\text{diff}} = (1 - m) \frac{c}{\pi}, \quad f_{\text{spec}} = \frac{D_{\text{GGX}} \cdot G_{\text{Smith}} \cdot F_{\text{Schlick}}}{4(\mathbf{n} \cdot \mathbf{v})_+ (\mathbf{n} \cdot \ell)_+}.$$

Here $\alpha = r^2$, $\mathbf{h} = \frac{\mathbf{v} + \ell}{\|\mathbf{v} + \ell\|}$ is the half-vector, and $F_0 = (1 - m) \cdot 0.04 + m \cdot c$. For complete expressions of D_{GGX} , G_{Smith} , and F_{Schlick} , we refer the reader to [26, 29, 33].

Neural Subsurface Residual. To model volumetric scattering, a learned residual term adds view- and light-dependent translucency:

$$C_{\text{sss}}(x) = \text{sss}(x) \cdot f_{\phi}(\mu(x), \Sigma(x), \mathbf{n}(x), \ell, \mathbf{v}),$$

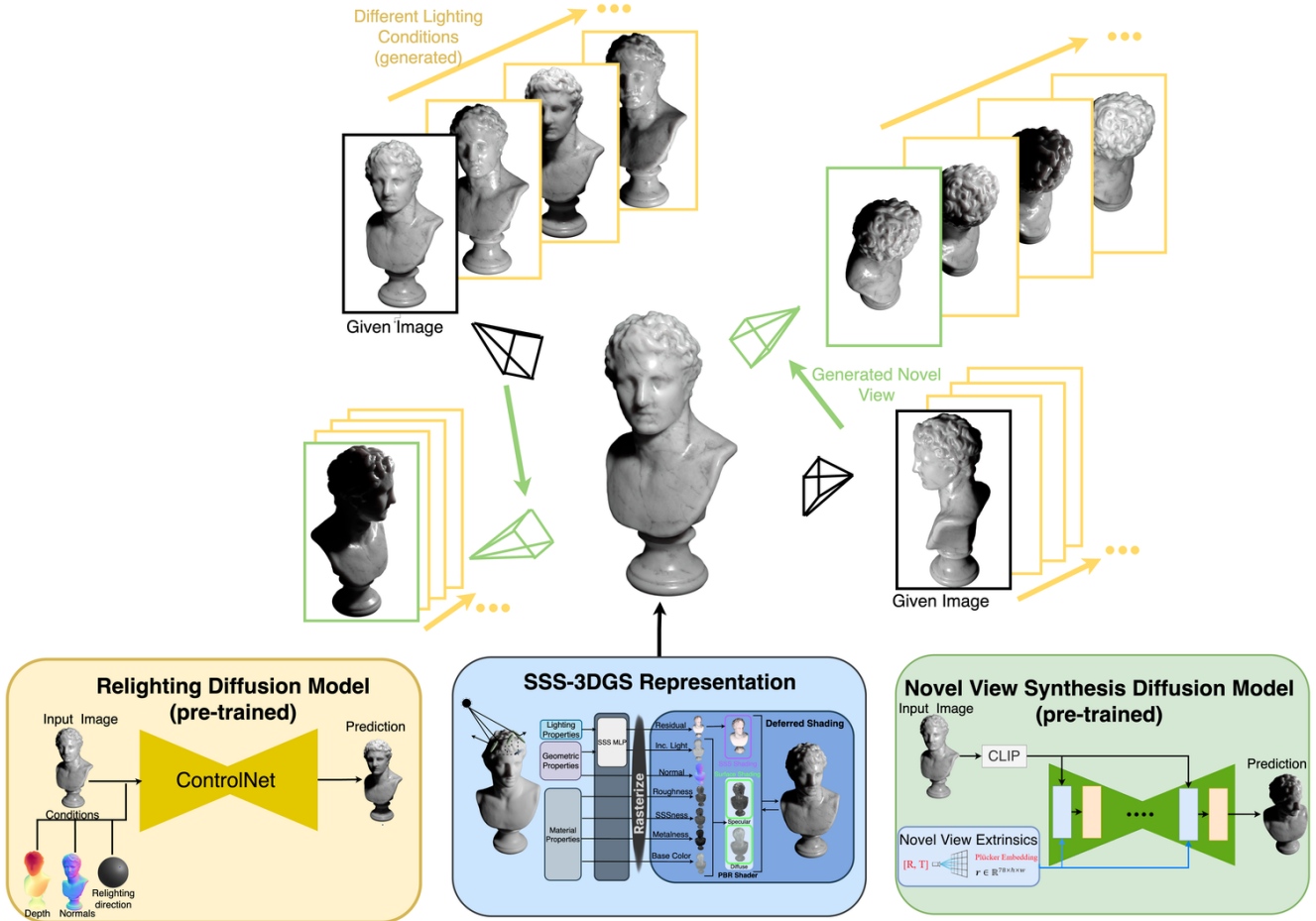


Figure 2. Overview of our data augmentation pipeline. From a few posed input images, we generate additional viewpoints using a novel-view diffusion model (green) and synthetic OLAT variants using a relighting model (yellow). The combined real and synthetic data are used to train SSS-3DGS [7] with an MLP for subsurface scattering, stabilized by our geometric consistency losses (Sec. 3.3).

where $sss(x) \in [0, 1]$ is a learned scalar controlling subsurface strength, and f_ϕ is a small MLP. This residual effectively encodes the radiance contribution of translucent transport for a single Gaussian, allowing for soft shadows, color bleeding, and glow effects beyond the surface BRDF.

3.2. Diffusion-Based Data Augmentation

To enable high-quality translucent reconstruction from sparse captures, we introduce a data-driven augmentation strategy based on pretrained diffusion models. We use these models synthesize photometrically plausible novel views and lighting conditions that supplement the limited input data during SSS-3DGS optimization (Sec. 3.1). Both diffusion models are fine-tuned once on a small subset of translucent objects and subsequently applied to all unseen objects, ensuring broad generalization without per-object retraining (Fig. 2). An extended discussion of the architecture and training procedure is provided in the Supplementary Material.

Fine-Tuning Strategy. We adapt two publicly available latent diffusion models for our purpose: one for novel-view synthesis (Free3D [45]) and one for relighting (inspired by ControlNet [40] and Poirier *et al.* [23]). Both were originally trained on large-scale datasets of predominantly opaque objects. To adapt them for translucent appearance effects, we fine-tune each model on *less than 7% of the total OLAT dataset* (see Sec. 4.1), using only a subset of images from four distinct translucent objects captured under controlled directional lighting and multiple viewpoints. All images used for fine-tuning are drawn exclusively from the training split, ensuring that no evaluation views or lights are seen by the diffusion models. Fine-tuning uses the original diffusion objectives with perceptual supervision (L1, SSIM, LPIPS) under fixed illumination and deterministic sampling, which encourages geometric consistency and reduces view-to-view drift. We discuss our finetuning strategy with more detail in the supplement, see Sec. C.

Novel-View Diffusion. For view synthesis, we employ fine-tune Free3D [45] architecture conditioned on the input image and camera pose through ray-conditioning normalization layers, without architectural modifications. The model learns to preserve object identity while improving parallax and silhouette coherence across novel viewpoints. During inference, it takes as input the source image and relative camera transformation and generates a geometrically consistent view from the target pose. The resulting synthetic views are used for photometric and geometric supervision during SSS-3DGS optimization.

Relighting Diffusion. For illumination augmentation, we extend the relighting model of Poirier-Ginter *et al.* [23] by enriching its conditioning. In addition to the source image, depth map, and target lighting code (encoded as 9D spherical harmonics), we also concatenate predicted surface normals [16] and depth [35]. Additional details are provided in Sec. C. Training follows the v -parameterization objective combined with perceptual (L1, SSIM, LPIPS), cycle-consistency, and blur-aware losses to encourage smooth irradiance transitions and stable light-transport behavior. This enables the synthesis of relit images that reproduce soft shadows, diffuse scattering, and low-frequency volumetric effects characteristic of translucent materials.

We emphasize that all conditioning maps are estimated automatically—no ground-truth normals or depths are required—making the pipeline applicable to casual or legacy captures.

3.3. Multi-View Geometric Consistency

To further improve Gaussian splatting reconstruction from diffusion-generated images—which may exhibit minor spatial or photometric inconsistencies inherent to generative synthesis (e.g., known geometric failures of diffusion models [24])—we introduce two illumination-invariant geometric losses. These consist of a silhouette consistency loss and a depth consistency loss that enforce cross-view structural alignment, thereby stabilizing optimization under both real and synthetic supervision. See Fig. 3 for an illustration.

Silhouette Consistency. For a pixel x in view i , we compute its 3D location X_i using depth $D_i(x)$ (which is obtained by using DepthAnythingv2 [35]) as well as its reprojection $x'_{i,j}$ to view j :

$$X_i = \pi_i^{-1}(x, D_i(x)), \quad x'_{i,j} = \pi_j(X_i), \quad (3.4)$$

where π_i is the projection function to view i . Using the soft silhouette in view i , computed from the Gaussian opacities:

$$S_i(x) = 1 - \prod_{k=1}^K (1 - \alpha_k(x)),$$

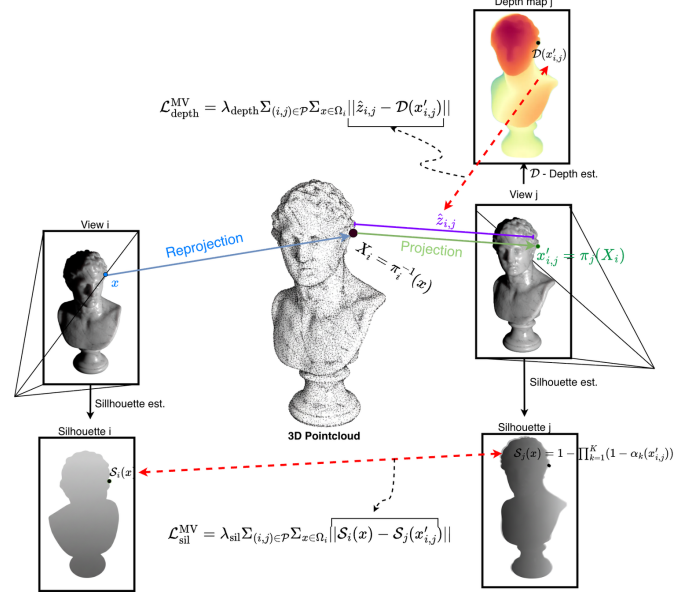


Figure 3. Visualization of the proposed geometric consistency losses. Silhouette consistency enforces cross-view contour alignment, while depth consistency stabilizes global geometry under varying lighting.

where $\alpha_k(x)$ is the opacity contribution at pixel x from the k -th 3D Gaussian, we define the multi-view silhouette consistency loss:

$$\mathcal{L}_{\text{sil}}^{\text{MV}} = \lambda_{\text{sil}} \sum_{(i,j)} \sum_{x \in \Omega_i} \|S_i(x) - S_j(x'_{i,j})\|_1. \quad (3.5)$$

This loss encourages consistent contours across views and improves boundary fidelity. See Fig. 3 for an illustration.

Depth Consistency. We additionally enforce cross-view agreement in depth. For back-projected point X_i (see Eq. (3.4)) and target camera center C_j , we compute:

$$\hat{z}_{i,j} = \|X_i - C_j\|_2, \quad x'_{i,j} = \pi_j(X_i),$$

and compare it with the rendered depth $D_j(x'_{i,j})$, computed with [35], defining the loss:

$$\mathcal{L}_{\text{depth}}^{\text{MV}} = \lambda_{\text{depth}} \sum_{(i,j)} \sum_{x \in \Omega_i} \|\hat{z}_{i,j} - D_j(x'_{i,j})\|_1. \quad (3.6)$$

This loss reduces floating geometry and improves global coherence.

Total Loss. Our final training objective extends Relightable 3D Gaussians (R3DGS) [9] by integrating diffusion-augmented supervision and our illumination-invariant geometric priors (Sec. 3.3). The total loss combines photometric, regularization, and geometric consistency

terms:

$$\begin{aligned}\mathcal{L}_{\text{total}} = & (1 - \lambda_{\text{dssim}})\mathcal{L}_1 + \lambda_{\text{dssim}}(1 - \text{SSIM}) + \lambda_{\text{lips}}\mathcal{L}_{\text{LPIPS}} \\ & + \lambda_{\text{mask}}\mathcal{L}_{\text{mask}} + \lambda_{\text{smooth}}\mathcal{L}_{\text{smooth}} + \lambda_{\text{enh}}\mathcal{L}_{\text{enh}} \\ & + \lambda_{\text{ray}}\mathcal{L}_{\text{ray}} + \lambda_{\text{sil}}\mathcal{L}_{\text{sil}}^{\text{MV}} + \lambda_{\text{depth}}\mathcal{L}_{\text{depth}}^{\text{MV}}.\end{aligned}\quad (3.7)$$

Here, $\mathcal{L}_{\text{photo}}$ is a combination of pixel-wise and perceptual losses (L1, SSIM, LPIPS) balancing structural and appearance fidelity. Regularization terms $\mathcal{L}_{\text{mask}}$, $\mathcal{L}_{\text{smooth}}$, \mathcal{L}_{enh} , and \mathcal{L}_{ray} follow prior work [9], enforcing spatial coherence, contrast preservation, and physical consistency in transmittance and shading.

3.4. DIAMOND-SSS Reconstruction Procedure

After fine-tuning, we freeze the diffusion models and use them to augment each scene before 3DGS optimization. For every real view, we synthesize 2–4 novel viewpoints, and for each real *and* synthetic view we generate 4–8 relit variants under novel OLAT conditions. This yields an expanded set of real images, diffusion-generated views, and synthetic relightings.

We then optimize a 3DGS model with an SSS residual on this augmented dataset. Photometric losses (L_1 , SSIM [34], LPIPS [42]) are applied to all images, with synthetic ones down-weighted by $\alpha = 0.5$ to mitigate diffusion artifacts. Geometric losses (multi-view silhouette and depth consistency) are applied uniformly to real and synthetic images to enforce cross-view structural alignment.

This joint supervision enables robust learning of both shape and appearance from as few as ten real captures per object, significantly reducing acquisition cost. Once adapted, the diffusion models can be reused for many reconstructions, enabling scalable capture of translucent materials in unconstrained settings.

4. Experiments

We evaluate DIAMOND-SSS on translucent object benchmarks following the SSS-3DGS dataset setup [7]. Our experiments are designed to validate three key aspects of our approach: (1) the effectiveness of diffusion-based augmentation for replacing real multi-light captures (Sec. 3.2), (2) the stabilizing effect of multi-view geometric consistency losses under sparse or synthetic supervision (Sec. 3.3), and (3) the overall reconstruction quality and data efficiency compared to state-of-the-art SSS reconstruction methods. A high-level overview of our pipeline is provided in Fig. 2 and detailed in Sec. 3.

Experimental Protocol. To analyze robustness under limited supervision, we adopt a **view–light pruning strategy**

inspired by prior work. Beginning with the full OLAT capture (~ 100 viewpoints, 112 lights per viewpoint), we progressively subsample camera poses and their associated illuminations while ensuring uniform coverage in pose–light space. This controlled reduction yields capture regimes ranging from full data to **3%** of views and lights, enabling us to quantify how reconstruction quality and geometric stability degrade across sparsity levels and to identify the practical breakpoints where competing methods fail.

We focus on six capture regimes that isolate each component of DIAMOND-SSS:

1. **All views, all lights:** ~ 100 views and 112 OLAT illuminations per viewpoint (probes the effect of geometric losses, Sec. 3.3).
2. **All views, 1 light per view:** ~ 100 views and 1 OLAT per view (tests diffusion-based relighting, Sec. 3.2).
3. **5% views, 5% lights:** $\sim 5\%$ of views and 5% of lights (joint sparse, tests both diffusion modules and geometric losses).
4. **3% views, 3% lights:** $\sim 3\%$ of views and 3% of lights (extreme sparse).
5. **5% views, full lights:** $\sim 5\%$ of views and all lights (tests diffusion novel-view synthesis, Sec. 3.2).
6. **3% views, full lights:** $\sim 3\%$ of views and all lights (extreme sparse views; isolates novel-view diffusion).

Following [7], all comparisons are made against SSS-3DGS, the strongest prior baseline. We omit KiloOSF [36] from our quantitative tables since it performs significantly below SSS-3DGS and our approach already surpasses this state-of-the-art method across all regimes.

4.1. Datasets

We use synthetic and real translucent objects from the SSS-3DGS dataset [7], captured under ~ 100 viewpoints and 112 one-light-at-a-time (OLAT) illuminations. To our knowledge, this is the only publicly available dataset with these characteristics. Objects include wax candles, jade figurines, plastic toys, and marble statues. For our six evaluation regimes, we subsample the original capture following the previously presented overview. Silhouettes are obtained from provided masks or automatic background subtraction. Depth and normal maps are estimated using off-the-shelf predictors: Depth Anything [35] and Marigold [16], respectively. These cues supervise our geometric consistency terms and condition the diffusion models (Secs. 3.2 and 3.3). In the supplementary material we present a visual overview of the dataset. As described in Sec. 3.2, both diffusion models are fine-tuned once using **≤ 7% of the total dataset**, drawn proportionally from four representative translucent objects (*car, jam jar, red candle, head*). This ensures robustness across material/transport variations while avoiding per-object retraining.

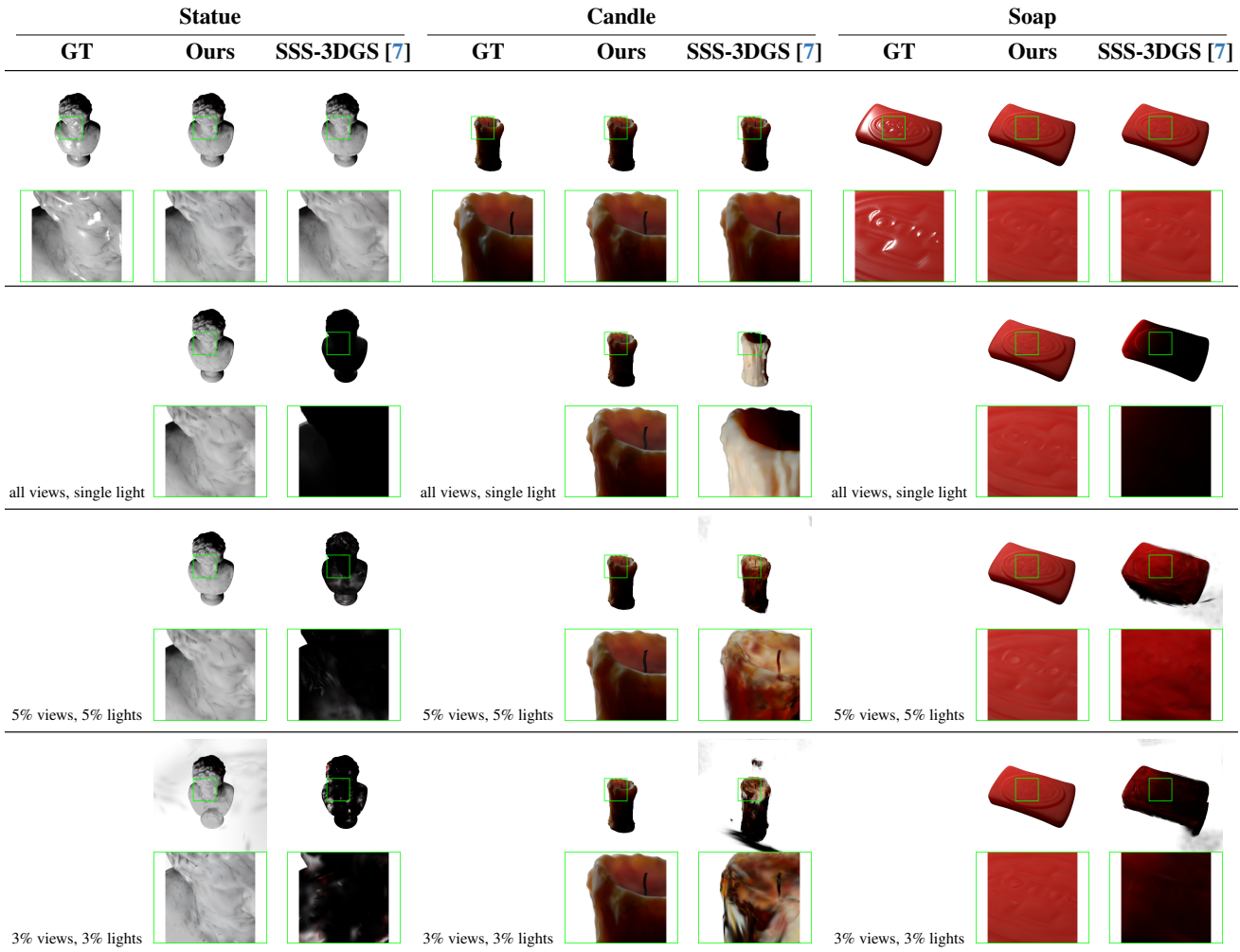


Figure 4. Qualitative comparison of reconstructed translucent appearance under different supervision conditions, the first row shows the setting: all views, all lights.

Regime	SSS-3DGS			DIAMOND-SSS (ours)		
	PSNR↑	SSIM↑	LPIPS↓	PSNR↑	SSIM↑	LPIPS↓
Full views, full lights	35.01	0.97	0.040	36.79	0.99	0.022
Full views, 1 light / view	21.94	0.88	0.177	35.14	0.98	0.030
5% views, 5% lights	20.10	0.64	0.215	24.56	0.89	0.035
3% views, 3% lights	18.15	0.58	0.319	21.34	0.86	0.039
5% views, full lights	25.32	0.86	0.060	32.15	0.96	0.020
3% views, full lights	25.32	0.86	0.060	31.31	0.96	0.020

Table 1. All capture regimes (compact). Metrics averaged over held-out test views/lights.

4.2. Implementation Details

We initialize 3D Gaussians from COLMAP reconstructions following [7]. Unless otherwise stated, each object is optimized with Adam (5×10^{-3} for Gaussian parameters, 1×10^{-3} for the MLP, decayed by 0.1 after 50k steps). The

SSS residual MLP has four layers with 64 hidden units and ReLU activations (see Sec. 3.1). A more detailed implementation road-map can be found in the Supplementary section, as well as a table with all the hyperparameters used.

Category	Variant	PSNR↑	SSIM↑	LPIPS↓
Geometric (10%, 3% lights)	w/o silhouette loss (Depth only)	20.697	0.621	0.331
	w/o depth loss (Silhouette only)	20.765	0.844	0.036
	w/o both (geom) (Vanilla)	20.222	0.591	0.319
	Full DIAMOND-SSS (Depth+Sil.)	21.342	0.853	0.039
Diffusion Augmentation (100% views, 1 light p/v)	w/o relighting diffusion	23.20	0.90	0.150
	w/o novel-view diffusion	35.05	0.98	0.031
	w/o both (diffusion)	23.10	0.90	0.152
	Full DIAMOND-SSS (Depth+Sil.)	35.14	0.98	0.030

Table 2. **Unified ablation of geometric consistency and diffusion augmentation.** Geometric losses are evaluated on *real data* (10% views, 3% lights), and diffusion variants on the *full views, 1 light per view* regime.

Diffusion-Based Augmentation. We fine-tune the official Free3D [45] checkpoint on our OLAT multi-view data using the original architecture, loss, and linear noise schedule ($0.00085 \rightarrow 0.0120$ over 1000 steps). We train for ~ 500 epochs with lr 1×10^{-4} , 100 warm-up steps, batches of 16 views from 4 objects, and 32×32 latents (scale 0.18215), using gradient checkpointing. Synthetic views are used during reconstruction with photometric losses down-weighted by $\alpha = 0.5$. For relighting, we adopt the implementation of Poirier-Ginter *et al.* [23], fine-tuning a ControlNet-style diffusion model conditioned on light direction to generate synthetic OLAT data from single-illumination captures. This augmented data trains a relightable 3DGS model with an MLP for light/view conditioning and per-image latent vectors for consistency.

Geometric Consistency. We implement the multi-view silhouette and depth consistency losses from Sec. 3.3 using depth-based reprojection: each pixel in a source view is back-projected into 3D, transformed into the target camera, and bilinearly sampled to obtain the corresponding silhouette and depth values. Consistency is enforced only on geometrically valid correspondences, filtered by visibility checks and per-pixel validity masks derived from depth reprojection. Silhouette alignment is supervised with a binary cross-entropy loss, and depth agreement with an ℓ_1 loss, both normalized by the number of valid pixels. Unless stated otherwise, we use weights $\lambda_{\text{sil}} = 0.5$ and $\lambda_{\text{depth}} = 0.3$.

4.3. Qualitative Results

Figure 4 compares reconstructions across the regimes. Under full supervision, SSS-3DGS already produces high-quality translucency, but suffers from slight geometric inconsistencies and blurry boundaries. Adding our geometric consistency losses (Sec. 3.3) sharpens silhouettes and improves depth coherence. As views and lights become sparse, the baselines exhibit strong degradation, whereas DIAMOND-SSS maintains realistic subsurface scattering, color bleeding, and soft shadows, particularly when diffusion-based re-

lighting (Sec. 3.2) is used to compensate for missing OLAT captures. More results are depicted in the Supplementary section.

4.4. Quantitative Results Across Capture Regimes

We report PSNR, SSIM, and LPIPS averaged over held-out views and illuminations. Tab. 1 consolidates all six regimes, comparing SSS-3DGS and DIAMOND-SSS. Across all data regimes, DIAMOND-SSS consistently improves fidelity—especially under sparse supervision—demonstrating that diffusion-based augmentation and geometric priors complement each other.

4.5. Data Efficiency and Ablations

We assess each component via ablations disabling geometric losses and/or diffusion augmentation (Table 2). Removing geometric consistency causes depth and silhouette drift, while omitting diffusion reduces photometric diversity and harms relighting. The full DIAMOND-SSS model offers the best stability-fidelity trade-off and consistently matches or surpasses SSS-3DGS, with the largest gains under sparse supervision (Tab. 1). Novel-view diffusion is particularly important when views are limited. Together with Fig. 4, these results show that diffusion-based relighting and geometric regularization enable high-quality translucent reconstruction with up to **90% less real data**. Additional qualitative ablations appear in the Supplementary section.

5. Limitations and conclusion

While DIAMOND-SSS achieves high-fidelity translucent reconstruction under sparse supervision, several limitations remain.

Diffusion realism. Diffusion-augmented views and relit samples, though visually consistent, are not strictly physically accurate and may exhibit slight color or scattering biases. Incorporating physics-based priors could enhance their realism.

Efficiency and scalability. Diffusion-based augmentation

adds computational cost, partly offset by reduced capture needs. Lighter architectures or shared scene-level finetuning may alleviate this overhead.

Conclusion. In summary, DIAMOND-SSS couples diffusion-based augmentation with geometric priors to achieve photometrically consistent, data-efficient reconstruction of translucent materials. It reduces real capture requirements by orders of magnitude while preserving quality, paving the way toward scalable acquisition of complex appearance in unconstrained settings.

6. Acknowledgments

This work was supported by the ERC Advanced Grant SIM-ULACRON and the Munich Center for Machine Learning (MCML). In addition, the work of G. Figueroa-Araneda was also supported by Universidad Técnica Federico Santa María and Centro Nacional de Inteligencia Artificial in Chile.

References

- [1] Mark Boss, Raphael Braun, Varun Jampani, Jonathan T. Barron, Ce Liu, and Hendrik P. A. Lensch. Nerd: Neural reflectance decomposition from image collections, 2021.
- [2] Mohammed Brahimi, Bjoern Haefner, Zhenzhang Ye, Bastian Goldluecke, and Daniel Cremers. Sparse views, near light: A practical paradigm for uncalibrated point-light photometric stereo. *IEEE/CVF Conference on Computer Vision and Pattern Recognition (CVPR)*, 2024.
- [3] Mohammed Brahimi, Bjoern Haefner, Tarun Yenamandra, Bastian Goldluecke, and Daniel Cremers. Supervol: Super-resolution shape and reflectance estimation in inverse volume rendering. In *IEEE/CVF Winter Conference on Applications of Computer Vision (WACV)*, 2024.
- [4] Brent Burley and Walt Disney Animation Studios. Physically-based shading at disney. In *International Conference on Computer Graphics and Interactive Techniques (SIGGRAPH)*, 2012.
- [5] Robert L. Cook and Kenneth E. Torrance. A reflectance model for computer graphics. *ACM Transactions on Graphics*, 1(1):7–24, 1982.
- [6] Eugene d’Eon and Geoffrey Irving. A quantized-diffusion model for rendering translucent materials. *ACM transactions on graphics (TOG)*, 30(4):1–14, 2011.
- [7] Jan-Niklas Dihlmann, Arjun Majumdar, Andreas Engelhardt, Raphael Braun, and Hendrik P. A. Lensch. Subsurface scattering for 3d gaussian splatting, 2024.
- [8] Craig Donner and Henrik Wann Jensen. A spectral bssrdf for shading human skin. *Rendering techniques*, 2006:409–418, 2006.
- [9] Jian Gao, Chun Gu, Youtian Lin, Zhihao Li, Hao Zhu, Xun Cao, Li Zhang, and Yao Yao. Relightable 3d gaussians: Realistic point cloud relighting with brdf decomposition and ray tracing. In *European Conference on Computer Vision*, pages 73–89. Springer, 2024.
- [10] Ruiqi Gao, Aleksander Hołyński, Philipp Henzler, Arthur Brussee, Ricardo Martin-Brualla, Pratul Srinivasan, Jonathan T Barron, and Ben Poole. Cat3d: create anything in 3d with multi-view diffusion models. In *Proceedings of the 38th International Conference on Neural Information Processing Systems*, pages 75468–75494, 2024.
- [11] Hanzhe Hu, Zhizhuo Zhou, Varun Jampani, and Shubham Tulsiani. Mvd-fusion: Single-view 3d via depth-consistent multi-view generation, 2024.
- [12] Steven L. Jacques. Optical properties of biological tissues: a review. *Physics in Medicine and Biology*, 58(11):R37–R61, 2013. Erratum in: *Phys Med Biol*. 2013 Jul 21;58(14):5007–5008. PMID: 23666068.
- [13] Henrik Wann Jensen, Stephen R Marschner, Marc Levoy, and Pat Hanrahan. A practical model for subsurface light transport. In *Proceedings of the 28th annual conference on Computer graphics and interactive techniques*, pages 511–518, 2001.
- [14] Haian Jin, Yuan Li, Fujun Luan, Yuanbo Xiangli, Sai Bi, Kai Zhang, Zexiang Xu, Jin Sun, and Noah Snavely. Neural gaffer: Relighting any object via diffusion, 2024.
- [15] Joanna Kaleta, Kacper Kania, Tomasz Trzcinski, and Marek Kowalski. Lumigauss: Relightable gaussian splatting in the wild. In *2025 IEEE/CVF Winter Conference on Applications of Computer Vision (WACV)*, pages 1–10. IEEE, 2025.
- [16] Bingxin Ke, Anton Obukhov, Shengyu Huang, Nando Metzger, Rodrigo Caye Daudt, and Konrad Schindler. Repurposing diffusion-based image generators for monocular depth estimation. In *Proceedings of the IEEE/CVF Conference on Computer Vision and Pattern Recognition (CVPR)*, 2024.
- [17] Bernhard Kerbl, Georgios Kopanas, Thomas Leimkühler, and George Drettakis. 3d gaussian splatting for real-time radiance field rendering, 2023.
- [18] Chenhao Li, Trung Thanh Ngo, and Hajime Nagahara. Inverse rendering of translucent objects using physical and neural renderers, 2023.
- [19] Ruoshi Liu, Rundi Wu, Basile Van Hoorick, Pavel Tokmakov, Sergey Zakharov, and Carl Vondrick. Zero-1-to-3: Zero-shot one image to 3d object. In *Proceedings of the IEEE/CVF international conference on computer vision*, pages 9298–9309, 2023.
- [20] Yuan Liu, Cheng Lin, Zijiao Zeng, Xiaoxiao Long, Lingjie Liu, Taku Komura, and Wenping Wang. Syncdreamer: Generating multiview-consistent images from a single-view image. In *The Twelfth International Conference on Learning Representations*, 2024.
- [21] Ben Mildenhall, Pratul P. Srinivasan, Matthew Tancik, Jonathan T. Barron, Ravi Ramamoorthi, and Ren Ng. Nerf: Representing scenes as neural radiance fields for view synthesis. In *European Conference on Computer Vision (ECCV)*, pages 405–421. Springer, 2020.
- [22] Bui Tuong Phong. Illumination for computer generated pictures. *Communications of the ACM*, 18(6):311–317, 1975.
- [23] Y. Poirier-Ginter, A. Gauthier, J. Philip, J.-F. Lalonde, and G. Drettakis. A diffusion approach to radiance field relighting using multi-illumination synthesis. *Computer Graphics Forum (Proc. Eurographics Symposium on Rendering)*, 43(4), 2024.

[24] Ayush Sarkar, Hanlin Mai, Amitabh Mahapatra, Svetlana Lazebnik, D. A. Forsyth, and Anand Bhattad. Shadows don't lie and lines can't bend! generative models don't know projective geometry...for now. In *Proceedings of the IEEE/CVF Conference on Computer Vision and Pattern Recognition (CVPR)*, pages 28140–28149, 2024.

[25] Kripasindhu Sarkar, Marcel C. Bühler, Gengyan Li, Daoye Wang, Delio Vicini, Jérémie Rivière, Yinda Zhang, Sergio Orts-Escolano, Paulo F. U. Gotardo, Thabo Beeler, and Abhimitra Meka. LitNeRF: Intrinsic radiance decomposition for high-quality view synthesis and relighting of faces. In *SIGGRAPH Asia*, 2023.

[26] Christophe Schlick. An inexpensive BRDF model for physically-based rendering. In *Proceedings of the Eurographics Workshop on Rendering*, pages 219–226, London, UK, 1994. Springer.

[27] Ruoxi Shi, Hansheng Chen, Zhuoyang Zhang, Minghua Liu, Chao Xu, Xinyue Wei, Linghao Chen, Chong Zeng, and Hao Su. Zero123++: A single image to consistent multi-view diffusion base model. *arXiv preprint arXiv:2310.15110*, 2023.

[28] Yichun Shi, Peng Wang, Jianglong Ye, Long Mai, Kejie Li, and Xiao Yang. Mvdream: Multi-view diffusion for 3d generation. In *The Twelfth International Conference on Learning Representations*, 2024.

[29] B. G. Smith. Geometrical shadowing of a random rough surface. *IEEE Transactions on Antennas and Propagation*, 15(5):668–671, 1967.

[30] Pratul P Srinivasan, Boyang Deng, Xiuming Zhang, Matthew Tancik, Ben Mildenhall, and Jonathan T Barron. NeRV: Neural reflectance and visibility fields for relighting and view synthesis. In *IEEE/CVF Conference on Computer Vision and Pattern Recognition (CVPR)*, 2021.

[31] Thomson TG, Jeppe Revall Frisvad, Ravi Ramamoorthi, and Henrik Wann Jensen. Neural BSSRDF: Object appearance representation including heterogeneous subsurface scattering. *arXiv*, 2023.

[32] TG Thomson, D. M. Tran, Henrik Wann Jensen, Ravi Ramamoorthi, and J. Frisvad. Neural sss: Lightweight object appearance representation. *Computer Graphics Forum*, 2024.

[33] Bruce Walter, Stephen R. Marschner, Hongsong Li, and Kenneth E. Torrance. Microfacet models for refraction through rough surfaces. In *Proceedings of the 18th Eurographics Symposium on Rendering (EGSR '07)*, pages 195–206, Aire-la-Ville, Switzerland, 2007. Eurographics Association.

[34] Zhou Wang, Alan C. Bovik, Hamid R. Sheikh, and Eero P. Simoncelli. Image quality assessment: From error visibility to structural similarity. *IEEE Transactions on Image Processing*, 13(4):600–612, 2004.

[35] Lihe Yang, Bingyi Kang, Zilong Huang, Zhen Zhao, Xiaogang Xu, Jiashi Feng, and Hengshuang Zhao. Depth anything v2. *Advances in Neural Information Processing Systems*, 37: 21875–21911, 2024.

[36] Hong-Xing Yu, Michelle Guo, Alireza Fathi, Yen-Yu Chang, Eric Ryan Chan, Ruohan Gao, Thomas Funkhouser, and Jiajun Wu. Learning object-centric neural scattering functions for free-viewpoint relighting and scene composition. *Transactions on Machine Learning Research (TMLR)*, 2023. arXiv:2303.06138.

[37] Jingyang Zhang, Yao Yao, Shiwei Li, Jingbo Liu, Tian Fang, David McKinnon, Yanghai Tsin, and Long Quan. Neilf++: Inter-reflectable light fields for geometry and material estimation, 2023.

[38] Kai Zhang, Fujun Luan, Qianqian Wang, Kavita Bala, and Noah Snavely. PhySG: Inverse rendering with spherical gaussians for physics-based material editing and relighting. In *IEEE/CVF Conference on Computer Vision and Pattern Recognition (CVPR)*, 2021.

[39] Kai Zhang, Fujun Luan, Zhengqi Li, and Noah Snavely. IRON: inverse rendering by optimizing neural sdfs and materials from photometric images. In *IEEE/CVF Conference on Computer Vision and Pattern Recognition (CVPR)*, 2022.

[40] Lvmin Zhang, Anyi Rao, and Maneesh Agrawala. Adding conditional control to text-to-image diffusion models. In *Proceedings of the IEEE/CVF International Conference on Computer Vision (ICCV)*, pages 3836–3847, 2023.

[41] Lvmin Zhang, Anyi Rao, and Maneesh Agrawala. Scaling in-the-wild training for diffusion-based illumination harmonization and editing by imposing consistent light transport. In *The Thirteenth International Conference on Learning Representations*, 2025.

[42] Richard Zhang, Phillip Isola, Alexei A. Efros, Eli Shechtman, and Oliver Wang. The unreasonable effectiveness of deep features as a perceptual metric. In *Proceedings of the IEEE Conference on Computer Vision and Pattern Recognition (CVPR)*, pages 586–595, 2018.

[43] Xiuming Zhang, Pratul P. Srinivasan, Boyang Deng, Paul E. Debevec, William T. Freeman, and Jonathan T. Barron. NeRFactor: neural factorization of shape and reflectance under an unknown illumination. *ACM Transactions on Graphics (TOG)*, 2021.

[44] Yuanqing Zhang, Jiaming Sun, Xingyi He, Huan Fu, Rongfei Jia, and Xiaowei Zhou. Modeling indirect illumination for inverse rendering. In *IEEE/CVF Conference on Computer Vision and Pattern Recognition (CVPR)*, 2022.

[45] Chuanxia Zheng and Andrea Vedaldi. Free3d: Consistent novel view synthesis without 3d representation. In *IEEE/CVF Conference on Computer Vision and Pattern Recognition (CVPR)*, pages 9720–9731, 2024.

[46] Shizhan Zhu, Shunsuke Saito, Aljaz Bozic, Carlos Aliaga, Trevor Darrell, and Christoph Lassner. Neural relighting with subsurface scattering by learning the radiance transfer gradient, 2023.

Supplementary Material

This Supplementary Material provides additional technical details, ablation studies, and qualitative evaluations that complement the main paper. Section A reports the full implementation details and hyperparameters for all modules in DIAMOND-SSS. Section B provides additional qualitative reconstructions under a wide range of capture regimes, demonstrating the robustness of DIAMOND-SSS, particularly in sparse-view and sparse-light settings where SSS-3DGS fails severely. Section C details the fine-tuning procedures for the diffusion-based components—multi-view and relighting diffusion—and presents extended qualitative comparisons against off-the-shelf NVS and relighting baselines. Section D expands on the formulation and practical considerations of the multi-view geometric losses, including visibility handling, depth normalization, sampling strategy, and targeted ablation studies on both synthetic and real objects. Finally, Section E summarizes compute requirements, reproducibility notes, and implementation considerations to facilitate future research and adoption.

A. Implementation and Hyperparameters

In this appendix we provide implementation and optimization details that complement the main paper (see Sec. 4.2).

A.1. Optimization and Training Schedule

We jointly optimize the 3D Gaussian parameters and the SSS residual MLP (see Sec. 3.1) using the Adam optimizer, with separate learning rates for geometry (5×10^{-3}) and appearance (1×10^{-3}). Both learning rates are reduced by a factor of 0.1 after 50k iterations. Training runs for 80k–100k steps depending on the object and capture regime.

Gaussian initialization, densification, and pruning follow the SSS-3DGS pipeline [7]. To ensure fair comparison across ablations, we keep the number of Gaussians fixed throughout optimization.

All experiments are implemented in PyTorch 2.2 with mixed precision and executed either on a single NVIDIA RTX A6000 (48 GB) or on a workstation equipped with a GPU with at least 24 GB VRAM, 32 GB RAM, and roughly 100 GB of disk space. The environment uses CUDA 11.6 for compatibility with our training framework.

A.2. Loss Weights

The main paper defines the full objective $\mathcal{L}_{\text{total}}$ in Sec. 3.3, combining photometric, regularization, and geometric consistency terms. For completeness, we summarize the scalar weights used in all experiments.

We employ a mixed photometric objective

$$\begin{aligned} \mathcal{L}_{\text{total}} = & (1 - \lambda_{\text{dssim}}) \mathcal{L}_1 + \lambda_{\text{dssim}} (1 - \text{SSIM}) + \lambda_{\text{lpips}} \mathcal{L}_{\text{LPIPS}} \\ & + \lambda_{\text{mask}} \mathcal{L}_{\text{mask}} + \lambda_{\text{smooth}} \mathcal{L}_{\text{smooth}} + \lambda_{\text{enh}} \mathcal{L}_{\text{enh}} \\ & + \lambda_{\text{ray}} \mathcal{L}_{\text{ray}} + \lambda_{\text{sil}} \mathcal{L}_{\text{sil}}^{\text{MV}} + \lambda_{\text{depth}} \mathcal{L}_{\text{depth}}^{\text{MV}}, \end{aligned} \quad (\text{A.1})$$

The regularization objective proposed in [7] combines several auxiliary losses that improve stability, material fidelity, and geometric consistency. First, a normal-consistency term enforces agreement between the predicted normals \mathbf{N} and pseudo-normals $\tilde{\mathbf{N}}$ derived from the rendered depth map D under a local planarity assumption:

$$\mathcal{L}_{\text{normals}} = \lambda_{\text{normals}} \|\mathbf{N} - \tilde{\mathbf{N}}\|_2. \quad (\text{A.2})$$

To supervise incident radiance, we constrain the clamped predicted illumination $\bar{L}_{\text{in}}(x, \omega_i)$ to match the learned spherical-harmonics visibility $V_{SH}(x, \omega_i)$ via an L1 loss

$$\mathcal{L}_{\text{incident}} = \lambda_{\text{incident}} \|\bar{L}_{\text{in}}(x, \omega_i) - V_{SH}(x, \omega_i)\|_1. \quad (\text{A.3})$$

Foreground consistency is enforced with a spatial masking loss, penalizing the contribution of Gaussians outside the image mask I_{mask} :

$$\mathcal{L}_{\text{mask}} = -\lambda_{\text{mask}} [I_{\text{mask}} \log(\alpha) + (1 - I_{\text{mask}}) \log(1 - \alpha)]. \quad (\text{A.4})$$

Material smoothness is encouraged using bilateral smoothing on metalness m , roughness r , subsurfaceness sss , and base color \mathbf{b} , each with its own weight $\lambda_{\text{smooth}}^{(q)}$; for a generic attribute PI_q the loss is

$$\mathcal{L}_{\text{smooth}}^{(q)} = \frac{1}{N} \sum_{x,y} M(x,y) \|\nabla PI_q(x,y)\| \exp(-\|\nabla I(x,y)\|), \quad (\text{A.5})$$

where $I(x, y)$ is the input image and $M(x, y)$ denotes the valid mask. To improve highlight and shadow reconstruction, the authors in [7] adopt the R3DGS enhancement loss [9], comparing the predicted base color \mathbf{b} to a pseudo-target T constructed from the input RGB image I_{rgb} using a sigmoid-based blending weight sw :

$$\begin{aligned} \mathcal{L}_{\text{enhance}} &= \lambda_{\text{enhance}} \|T - \mathbf{b}\|_1, \\ T &= sw \cdot I_{rgb}^2 + (1 - sw) \cdot [1 - (1 - I_{rgb})^2]. \end{aligned} \quad (\text{A.6})$$

Finally, we supervise learned visibility using ray-traced ground-truth visibility V_{RT} :

$$\mathcal{L}_{\text{raytrace}} = \lambda_{\text{raytrace}} \|V_{SH}(x, \omega_i) - V_{RT}(x, \omega_i)\|_1. \quad (\text{A.7})$$

Together, these terms form the complete regularization objective used during optimization. All hyperparameters used in our experiments are presented in Tab. 3.

A.3. Hyperparameter Tuning

The goal in this section is to understand how different configurations affect the custom objective $\mathcal{L}_{\text{total}}$ (see Eq. A.1), which aggregates photometric and regularization terms into a single performance metric for translucent scenes.

A.3.1. Parallel Coordinate Analysis

Figure 5 shows a parallel coordinate plot where each polyline corresponds to one hyperparameter configuration, and each vertical axis represents a different hyperparameter. The color encodes performance: lighter lines denote higher $\mathcal{L}_{\text{total}}$ (better configurations), while darker lines correspond to lower-performing settings.

Several trends emerge:

- Mid-range values of λ_{dssim} (0.25, 0.3) and $\lambda_{\text{incident.light}}$ (0.01–0.012) tend to perform best, suggesting that moderate weighting of structural similarity and incident-light regularization provides a good trade-off for reconstruction quality.
- Higher values of λ_{normal} (0.045 $>$) and $\lambda_{\text{base.color.smooth}}$ (0.018 $>$) correlate with better performance, indicating that emphasizing surface consistency and base-color smoothness can enhance overall fidelity.
- For $\lambda_{\text{roughness.smooth}}$ (0.002 $<$) and $\text{densify.until_iter}$ (10K $<$), the best configurations cluster towards lower values, suggesting that overly strong roughness smoothing or excessively long densification phases can harm fine detail and lead to suboptimal reconstructions.

Overall, these patterns provide guidance on how to balance detail preservation, smoothness, and physical plausibility in SSS-3DGS-style reconstructions.

A.3.2. Best Configuration vs. Original

Table 4 compares the original hyperparameter configuration from [7] with the best-performing combination identified by our tuning procedure.

A few observations:

- The perceptual loss weight λ_{lpips} decreases from 0.2 to 0.171, suggesting that a slightly reduced emphasis on perceptual similarity can improve the aggregate objective when combined with other terms.
- In contrast, the structural loss weight λ_{dssim} increases substantially from 0.2 to 0.492, indicating that stronger structural supervision plays a key role in achieving better reconstructions.
- The normal-consistency term λ_{normal} is tuned upward from 0.02 to 0.037, reinforcing the benefit of encouraging local surface coherence.
- Among regularization terms, $\lambda_{\text{metallic.smooth}}$ and $\lambda_{\text{roughness.smooth}}$ increase, whereas $\lambda_{\text{base.color}}$ and $\lambda_{\text{base.color.smooth}}$ are slightly reduced. This suggests

that more flexible modeling of specular behavior combined with milder regularization on base color yields better fidelity.

- The densification strategy favors a shorter and more aggressive phase: `densify.until_iter` is reduced from 15000 to 10000, `densification.interval` is slightly increased, and `densify.grad_threshold` is relaxed. The opacity reset interval is also reduced from 3000 to 1000. Together, these changes promote faster adaptation of the Gaussian set and help avoid early overfitting.

Overall, the tuned configuration reflects a nuanced rebalancing of perceptual, structural, and regularization terms, leading to improved performance under the aggregated objective $\mathcal{L}_{\text{total}}$ while remaining close in spirit to the original SSS-3DGS design.

B. Additional Qualitative Reconstructions

To complement the quantitative evaluations presented in the main paper, we provide additional qualitative reconstructions across a variety of translucent objects and capture regimes. These visual comparisons illustrate how DIAMOND-SSS behaves under different levels of supervision, ranging from full-view OLAT captures to extremely sparse pose–light subsets.

Comparison across objects and capture regimes. Figure 6 presents reconstructions for three representative objects—*Plastic Bottle*, *Crystal*, and *Massage Ball*—under four supervision levels: (i) all views and all lights, (ii) all views with a single light per view, (iii) 5% of views and 5% of lights, and (iv) 3% of views and 3% of lights.

In all settings, DIAMOND-SSS produces sharper boundaries, more stable silhouettes, and more faithful subsurface-scattering cues than SSS-3DGS [7]. In the sparse regimes (5%/5% and 3%/3%), SSS-3DGS fails severely—exhibiting strong boundary leakage, collapsed geometry, and inconsistent opacity—while DIAMOND-SSS remains stable and reconstructs the correct translucent appearance.

Fine-grained appearance comparisons. Figure 7 provides additional close-up views highlighting translucent appearance, color diffusion, and internal glow. Across objects, DIAMOND-SSS preserves the soft radiance falloff characteristic of translucent materials while maintaining geometric fidelity. In contrast, SSS-3DGS often exhibits noisy silhouettes, incorrect color bleeding near boundaries, or inconsistent opacity when supervision becomes sparse.

These qualitative results reinforce the core claim of the paper: by integrating diffusion-based augmentation with multi-view geometric consistency, DIAMOND-SSS remains

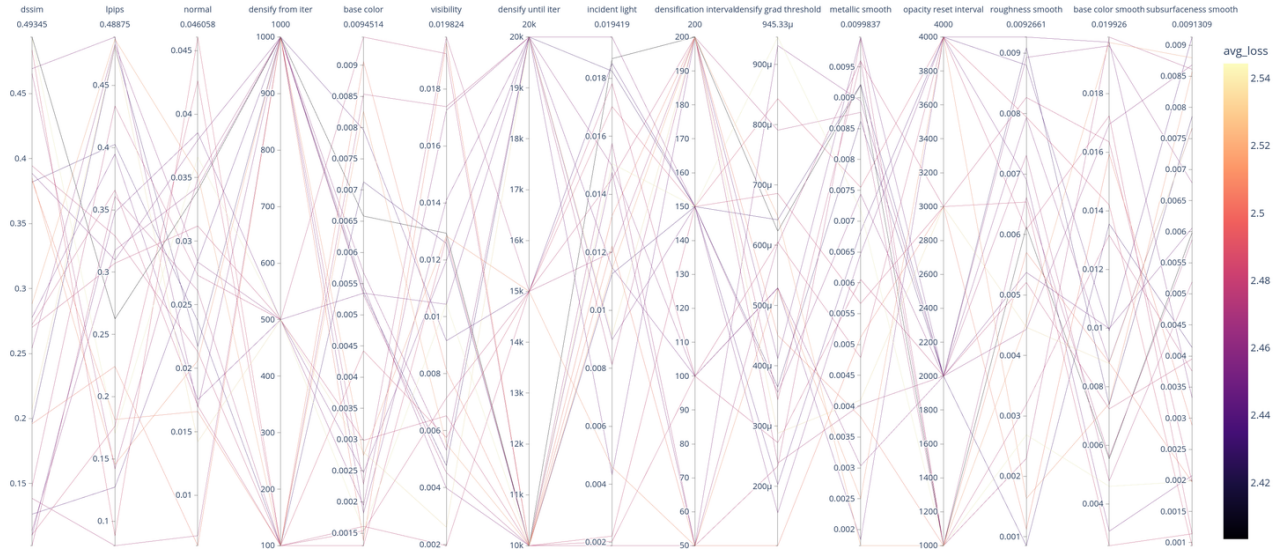


Figure 5. **Parallel coordinate plot of the hyperparameter search.** Each line corresponds to one configuration; lighter colors indicate higher values of the aggregated objective $\mathcal{L}_{\text{total}}$, as defined in Eq. A.1.

Training and learning rate parameters		Densification and loss parameters	
Configuration	Value [7]	Configuration	SValue
iterations	10,000	percent_dense	0.01
batch size	4	densification_interval	150
Gaussian learning rate	5×10^{-3}	opacity_reset_interval	3000
MLP learning rate	1×10^{-3}	densify_from_iter	500
position_lr_init	0.00016	densify_until_iter	10000
position_lr_final	0.0000016	densify_grad_threshold	0.0010
position_lr_delay_mult	0.01	densify_grad_normal_threshold	—
position_lr_max_steps	30,000	normal_densify_from_iter	0
normal_lr	0.01	random_background	False
normals_lr	0.01	sss_width	32
sh_lr	—	λ_{dssim}	0.492
feature_lr	0.0025	λ_{lpips}	0.171
color_lr	0.0025	λ_{mask}	0.1
opacity_lr	0.05	λ_{smooth}	[0.002, 0.002, 0.002, 0.006]
scaling_lr	0.005	λ_{enh}	0.005
rotation_lr	0.001	λ_{ray}	0.01
env_lr	0.1	λ_{sil}	0.5
env_rest_lr	0.001	λ_{depth}	0.3
base_color_lr	0.01	α (synthetic weight)	0.5
roughness_lr	0.01	λ_{normal}	0.037
metallic_lr	0.01	$\lambda_{\text{visibility}}$	0.01
subsurfaceness_lr	0.01	$\lambda_{\text{incident_light}}$	0.015
light_lr	0.001	$\lambda_{\text{mask_entropy}}$	0.1
light_rest_lr	0.0001	$\lambda_{\text{base_color}}$	0.002
light_init	-1.0	$\lambda_{\text{base_color_smooth}}$	0.005
visibility_lr	0.0025	$\lambda_{\text{metallic_smooth}}$	0.007
visibility_rest_lr	0.0025	$\lambda_{\text{roughness_smooth}}$	0.003
sss_lr	0.001	$\lambda_{\text{subsurfaceness_smooth}}$	0.002

Table 3. **DIAMOND-SSS configuration** Training and densification hyperparameters for DIAMOND-SSS.

robust even under highly incomplete OLAT captures, provid-

ing state-of-the-art reconstructions of translucent materials.

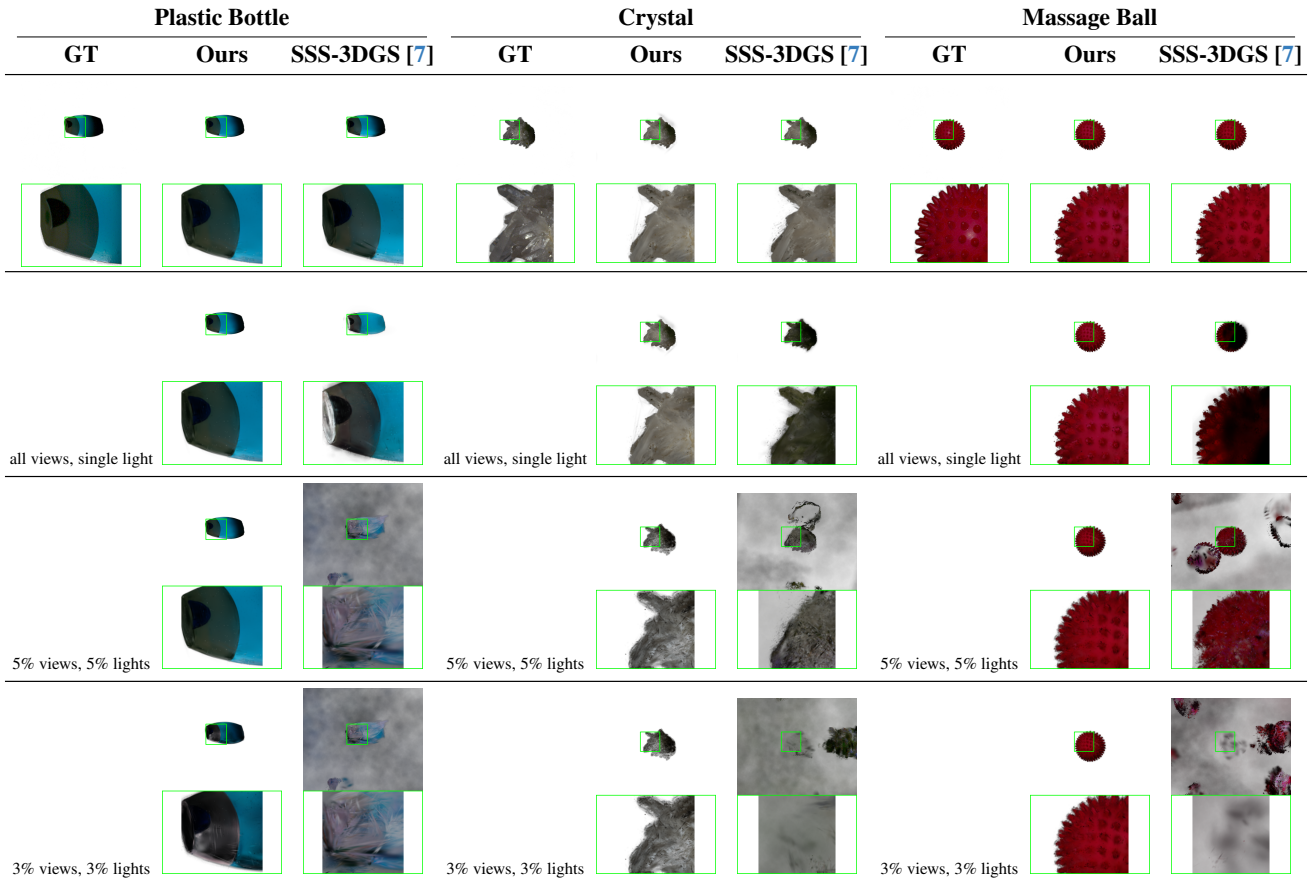


Figure 6. Qualitative comparison of reconstructed translucent appearance under different supervision conditions, the first row shows the setting: all views, all lights.

Hyperparameter	Original	Best
λ_{dssim}	0.200	0.492
λ_{lips}	0.200	0.171
λ_{normal}	0.020	0.037
$\lambda_{visibility}$	0.010	0.010
$\lambda_{incident_light}$	0.020	0.015
λ_{base_color}	0.005	0.002
$\lambda_{base_color_smooth}$	0.006	0.005
$\lambda_{metallic_smooth}$	0.002	0.007
$\lambda_{roughness_smooth}$	0.002	0.003
$\lambda_{subsurfaceness_smooth}$	0.002	0.002
densification_interval	100	150
opacity_reset_interval	3000	1000
densify_from_iter	500	500
densify_until_iter	15000	10000
densify_grad_threshold	0.0002	0.0010

Table 4. **Original vs. tuned hyperparameter configuration.** The “Best” setting corresponds to the highest \mathcal{L}_{total} found in our search, as illustrated in Fig. 5.

C. Diffusion Fine-Tuning Details

The diffusion-based augmentation pipeline is introduced in Sec. 3.2 and integrated into the reconstruction procedure in Sec. 3.4. Here we provide additional training and conditioning details for the two diffusion models used in DIAMOND-SSS: a multi-view (novel-view) diffusion model and a re-lighting diffusion model. Both models are fine-tuned once on a small OLAT subset and are then reused across all test objects and capture regimes, without any per-object retraining.

C.1. Training Data for Diffusion Models

Figure 8 shows an overview of the dataset and Fig. 9 depicts the OLAT capture setup used by [7] to generate the dataset. As described in Secs. 4.1 and 4.2, both diffusion models are fine-tuned on a small subset ($\leq 7\%$) of the full OLAT training data from SSS-3DGS [7]. We select four representative translucent objects—*red car*, *jam jar*, *wax candle*, and *marble head*—covering a range of scattering behaviors and specularities.

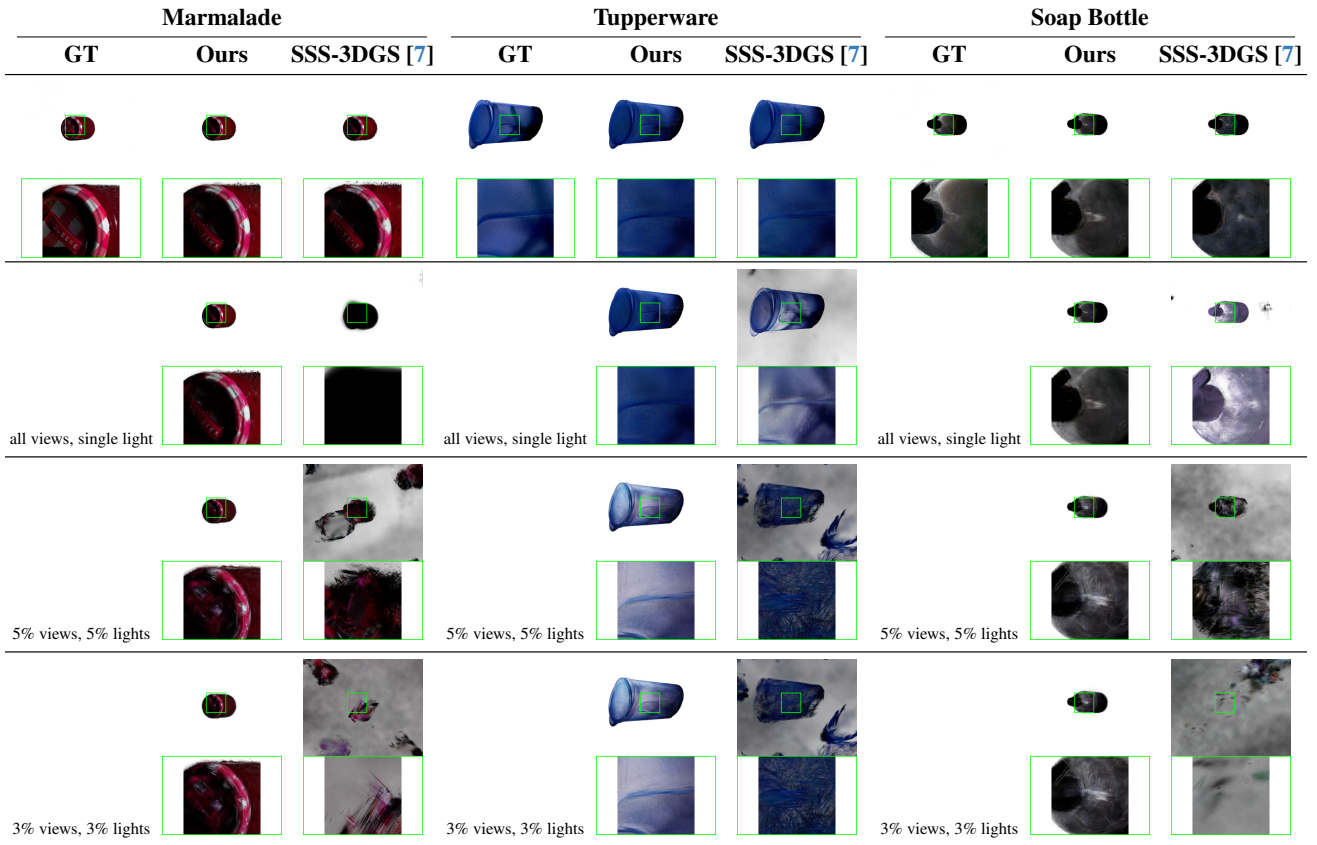


Figure 7. Qualitative comparison of reconstructed translucent appearance under different supervision conditions, the first row shows the setting: all views, all lights.

We emphasize that:

- Fine-tuning uses only training views and illuminations; no evaluation frames are seen by the diffusion models.
- The same fine-tuned models are reused across *all* test objects and capture regimes (no per-object or per-regime retraining).
- Illumination is kept fixed for multi-view diffusion (to isolate geometry) and view is kept fixed for relighting diffusion (to isolate light transport).

Together, these two diffusion models are used to expand a sparse OLAT capture into a denser multi-view, multi-illumination training set for DIAMOND-SSS.

C.2. Multi-View Diffusion (Novel-View Synthesis)

Purpose and model selection. Given a reference image I_{v_r} from viewpoint v_r and a target pose $P_v = (K, T_v)$, the multi-view diffusion module synthesizes the corresponding novel view \hat{I}_v . This densifies the camera trajectory under fixed illumination, enabling cross-combination with the relighting module to obtain synthetic multi-view, multi-light supervision within DIAMOND-SSS.

We first benchmarked several diffusion-based NVS mod-

els in inference mode—Zero123 [19], Zero123++ [27], MVD-Fusion [11], and Free3D [45]. On SSS-3DGS OLAT data, Free3D showed the strongest geometry and silhouette consistency out of the box, and we adopt it as our baseline prior. Representative comparisons are provided in Figs. 10 to 12. See Fig. 2 for an overview of the architecture.

Training procedure. We fine-tune the official Free3D checkpoint [45] (latent-diffusion UNet, 32×32 latents, scaling 0.18215) using the original denoising objective and linear noise schedule ($0.00085 \rightarrow 0.0120$ over 1000 steps). Training sequences are sampled under fixed illumination so that the model learns geometric variation without entangling lighting.

Camera poses are injected through ray-conditioning normalization layers, and lightweight multi-view attention and noise-sharing modules promote cross-view consistency. No architectural changes are introduced; only the weights are adapted to the OLAT domain.

Fine-tuning hyperparameters:

- **Batch size:** 16 target views sampled from 4 distinct objects,

- **Learning rate:** 1×10^{-4} with 100 warm-up steps,
- **Training duration:** ≈ 500 epochs on the OLAT subset,
- **Memory optimization:** Gradient checkpointing enabled.

Use within DIAMOND-SSS. During reconstruction, synthetic views generated by the multi-view diffusion module are rendered through the same camera poses as real observations. Photometric losses on synthetic images are down-weighted by the factor α defined in Sec. 3.4, while geometric consistency losses (e.g., silhouette or depth consistency) benefit fully from the increased viewpoint density.

C.3. Relighting Diffusion

Purpose and model selection. Given a single-view RGB input I_{v,l_s} under source illumination l_s , together with auxiliary conditioning maps C_v (depth and normals), the relighting diffusion module predicts the same view under a novel target light l_{tgt} . This expands the illumination coverage under fixed geometry and is especially useful in regimes such as “all views, 1 light per view,” where synthetic OLAT variants provide dense lighting supervision.

We adopt a ControlNet-style conditional diffusion framework inspired by [23, 40], starting from the public implementation of Poirier-Ginter *et al.* [23]. An architectural overview is included in Fig. 2.

Training procedure. We augment the model original model to receive the following conditioning signals:

- **Source RGB image:** I_{v,l_s} ,
- **Estimated depth map:** from Depth Anything v2 [35],
- **Estimated surface normals:** from Marigold [16],
- **Target illumination:** 9D spherical harmonic encoding $\Phi(l_{tgt})$.

Depth and normals are resized and normalized to match the UNet resolution. SH features are injected into both the ControlNet branch and the denoiser’s timestep and cross-attention embeddings. The architecture itself is unchanged; only the training data and conditioning inputs are adapted to OLAT captures. In Fig. 13 depicts examples of the conditions used per object.

Training objective. We employ the v -parameterization objective combined with a mixture of L1, SSIM, and LPIPS losses, as well as cycle-consistency and blur-aware terms to encourage stable low-frequency light transport and reduce high-frequency artifacts. Training samples follow:

$$(I_{v,l_s}, D_v, N_v, \Phi(l_{tgt}), I_{v,l_{tgt}}),$$

where $I_{v,l_{tgt}}$ is the corresponding OLAT ground truth. The implementation follows [23], with modifications only to the data and conditioning.

Use within DIAMOND-SSS. During reconstruction, the relighting diffusion module produces synthetic OLAT variants for each view. As with multi-view diffusion outputs, synthetic photometric losses are down-weighted by α , but these augmented illuminations still contribute meaningfully to multi-view silhouette and depth consistency, improving supervision across illumination conditions.

C.4. Setup: Use with Real, Relighted, and Fully Synthetic Data

Real OLAT captures. We use native OLAT images with provided (K_v, T_v) without modification.

Relighting augmentation. For settings such as “all views, 1 light per view,” missing illuminations are synthesized using the relighting diffusion model (Sec. C.3). The camera parameters (K_v, T_v) remain unchanged.

Fully synthetic multi-view sets. When using multi-view diffusion + relighting, we generate:

- novel poses P_v from the Free3D-based NVS model (Sec. C.2),
- relighted OLAT equivalents under all target directions. Generated data is aligned with the original OLAT lattice (same lights, comparable poses).

C.5. Benchmarking and ablation studies

We evaluate the effect of diffusion fine-tuning for both the multi-view synthesis module and the relighting module. Figures 10–12 summarize the multi-view synthesis behavior across several baselines, while Figures 14 and 15 focus on the relighting model. In addition, Table 2 shows our numerical results for the ablation studies.

Multi-view diffusion (NVS). We compare our fine-tuned Free3D model with: (1) off-the-shelf Free3D, (2) Zero123, (3) Zero123-XL, and (4) MVD-Fusion.

Across synthetic and real objects (Figures 10, 11, 12), our fine-tuned model consistently produces:

- sharper and more stable silhouettes,
- reduced geometric drift across viewpoints,
- fewer distortions in thin structures,
- better preservation of object identity under large viewpoint changes.

This justifies using Free3D as the backbone for DIAMOND-SSS and highlights the importance of domain adaptation to OLAT capture conditions.

Relighting diffusion. We further ablate the effects of progressively increasing conditioning and supervision:

1. Baseline RGB-only conditioning,
2. + depth and normal conditioning,

3. + L1 and perceptual losses.

As illustrated in Figures 14 and 15, each addition improves physical realism:

- depth improves global shadow placement,
- normals sharpen high-frequency surface cues,
- perceptual losses reduce haloing and over-sharp reflections,
- the full model best reproduces soft-scattering cues, achieving smooth light transitions characteristic of SSS material appearance.

Summary. The ablations show that diffusion models benefit substantially from fine-tuning under our OLAT dataset and conditioning strategy. For NVS, fine-tuning improves geometric coherence and silhouette stability. For relighting, deeper conditioning leads to more faithful subsurface-scattering behavior and reduced artifacts. These findings support the design choices adopted in DIAMOND-SSS and demonstrate that diffusion-based augmentation becomes reliable only after domain adaptation.

D. Multi-View Geometric Losses: Practical Details

The multi-view geometric consistency losses introduced in Sec. 3.3—namely multi-view silhouette consistency and multi-view depth consistency—play a central role in stabilizing reconstructions under sparse or synthetic supervision. This section provides additional implementation details, motivation, and qualitative analyses that complement the main text.

D.1. Motivation and Intuition

Multi-view photometric supervision alone does not sufficiently constrain the geometry of translucent objects, in particular in our very sparse setting with synthetic data augmentation. Small inconsistencies in predicted depth or occupancy can lead to view-dependent artifacts, such as boundary bleeding or inconsistent surface placement, which propagate into both shading and appearance, especially under SSS transport.

The two geometric consistency terms complement each other:

Silhouette Consistency. The silhouette-consistency term enforces that pixels corresponding to the object’s foreground in one view remain foreground when reprojected into another view. Concretely, for a pixel x in view i , we back-project it using its predicted depth and reproject it into view j (see Eq. (3.5)). The loss penalizes cases where this reprojected point falls outside the soft silhouette mask of view j , thereby stabilizing object boundaries, reducing opacity

bleeding, and improving cross-view alignment of object outlines.

Depth Consistency. Silhouette alignment alone does not provide depth information. The depth consistency loss addresses this by enforcing agreement between the predicted metric depth in view j and the back-projected/reprojected depth from view i (see Eq. (3.6) in the main paper). This ensures that the same physical surface point occupies a consistent 3D position across camera viewpoints, thereby improving global geometric coherence.

Together, these losses constrain both *where* the surface should appear (silhouette) and *how far* it should lie along each viewing ray (depth), reducing cross-view inconsistencies and improving stability under downstream relighting.

D.2. Visibility and Correspondence Filtering

Both $\mathcal{L}_{\text{sil}}^{\text{MV}}$ and $\mathcal{L}_{\text{depth}}^{\text{MV}}$ rely on correspondences obtained via back-projection from a source view i to a target view j using the camera models. In practice, we improve robustness by:

- **Domain filtering:** Correspondences whose reprojected coordinates $x'_{i,j}$ fall outside the target image plane are discarded.
- **Silhouette filtering:** Pixels reprojected outside the target soft silhouette (beyond a small tolerance) are ignored.
- **Depth validity:** Correspondences with invalid or missing depth (e.g., occlusions or empty space) in either view are removed.
- **Normalization:** Each loss term is normalized by the number of valid correspondences to avoid biasing toward dense or front-facing views.

This visibility-aware masking substantially reduces artifacts near occlusion boundaries and improves stability in sparse-view settings.

D.3. Depth Normalization and Numerical Stability

Depth values depend on the scene scale and camera intrinsics. To improve numerical conditioning, both the reprojection depth $\hat{z}_{i,j}$ and the rendered depth $D_j(x')$ are linearly normalized to $[0, 1]$ using scene-specific near/far clipping planes. This removes the need for per-object tuning of λ_{depth} and yields consistent gradients across scenes.

D.4. Ablation Studies

We evaluate the contribution of each multi-view geometric term through controlled ablations on synthetic and real OLAT data. The quantitative results are summarized in Table 2, and qualitative comparisons appear in Figures 16–21.

Silhouette-only supervision. Adding only the silhouette consistency term improves boundary alignment by ensuring that reprojected points fall within the target-view silhouette.

As shown in Figure 16 (second column), this reduces edge bleeding and stabilizes contours but does not fully resolve metric inconsistencies.

Depth-only supervision. The depth consistency loss enforces agreement between the reprojected depth $\hat{z}_j(X)$ and the rendered depth $D_j(x')$ in the target view. Figure 16 (third column) shows that this significantly reduces geometric drift across views, improving spatial coherence even in sparse-view settings.

Combined silhouette + depth supervision. Using both terms yields the most stable reconstructions. As seen in Figures 16 (fourth column) and 17, the combination delivers accurate geometry and clean boundaries, with fewer view-dependent artifacts than either component alone.

Generalization across objects. Figures 18 and 19 demonstrate that these improvements generalize across diverse synthetic and real objects, including highly translucent materials. The combined loss consistently produces sharper silhouettes and more metrically consistent shapes.

Isolated silhouette effects. Figures 20 and 21 highlight the specific gain from silhouette consistency alone—most notably the suppression of boundary haloing and improved contour sharpness.

Summary. Across all experiments, multi-view geometric supervision (i) sharpens boundaries, (ii) improves metric alignment, and (iii) reduces view-dependent distortions. These trends match the improvements reported quantitatively in Table 2 and play a central role in the reliability of DIAMOND-SSS under sparse or noisy view regimes.

E. Reproducibility and Compute

DIAMOND-SSS is built entirely on publicly released components in 3D Gaussian Splatting and diffusion architectures. To facilitate reproducibility, we summarize below the practical considerations, compute settings, and implementation choices that complement the hyperparameters in Tab. 3 and the training details provided in Secs. C and 4.2.

Hardware. All experiments were conducted on a single NVIDIA RTX A6000 GPU (49 GB VRAM) using PyTorch 2.2 with automatic mixed precision. A local workstation with 32 GB RAM and \sim 100 GB of disk storage (datasets, checkpoints, intermediate outputs) is sufficient to reproduce every experiment. Training the Free3D fine-tuning and the relighting model does not require multi-GPU setups.

Code base. Our implementation builds on:

- 3DGS [17] for the base Gaussian renderer,
- Relightable 3DGS [9] for material and lighting branches,
- SSS-3DGS [7] for subsurface-scattering modeling,
- Free3D [45] for multi-view diffusion,
- Poirier-Ginter et al. [23] for relighting diffusion (ControlNet-style conditioning).

All components required to reproduce our results are open source.

Training schedule and runtime. Reconstruction of each scene (including multi-view geometric consistency) requires approximately:

- **1–1.5 hour** for **full-view** OLAT settings,
- **0.5–1 hours** for **sparse-view** settings,

measured on an RTX A6000. Fine-tuning the diffusion models is performed once:

- **Free3D NVS fine-tuning:** \approx 15 hours for 500 epochs,
- **Relighting model:** \approx 12–20 hours depending on object subset size.

These models are then reused for all experiments without per-object retraining.

Scene reuse and caching. Rendered depth, normals, and intermediate diffusion results are cached to reduce repeated compute. Gaussian densification schedules and multi-view loss masks (Sec. D) are shared across experiments to ensure comparability.

Randomness and determinism. All experiments use fixed seeds for camera sampling, appearance model initialization, and diffusion noise, ensuring repeatability with no run-to-run variations.

Reconstruction pipeline consistency. Evaluation scripts, loss computation, and image-space metrics (PSNR, SSIM, LPIPS) follow the same routines across synthetic and real scenes for consistent reporting.

Overall, DIAMOND-SSS can be reproduced on a single high-memory GPU and relies only on publicly available components. The training schedules, hyperparameters, and data augmentations are fully documented in the main paper and this supplementary material.

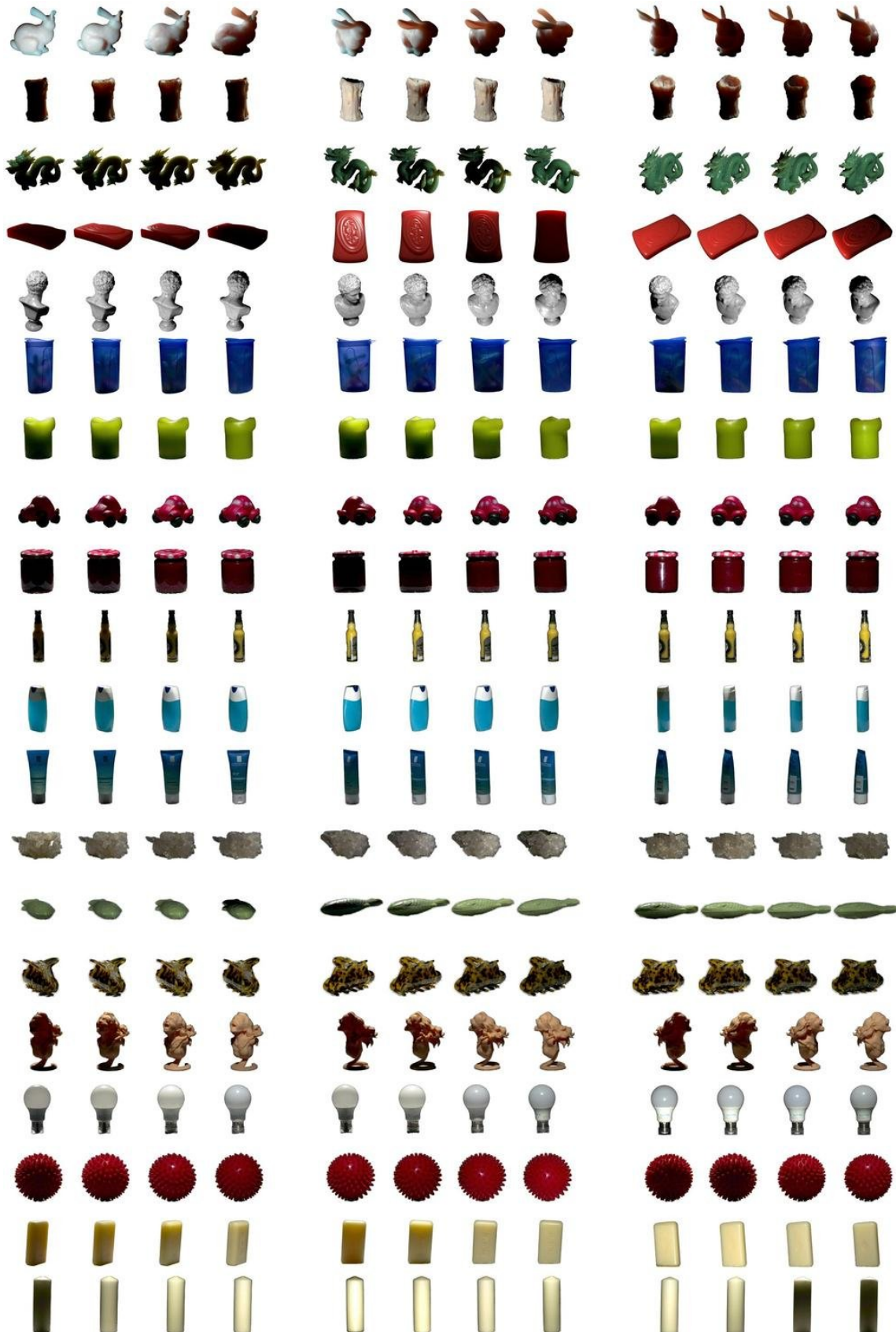


Figure 8. Dataset overview showing synthetic (top) and real (bottom) objects under different illumination and viewpoints.

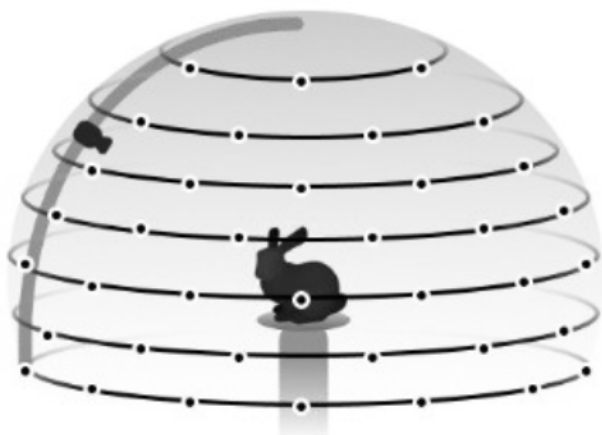


Figure 9. Overview of OLAT capture setup. A hemispherical lighting rig sequentially illuminates the object with one light at a time, capturing per-light images from fixed viewpoints.

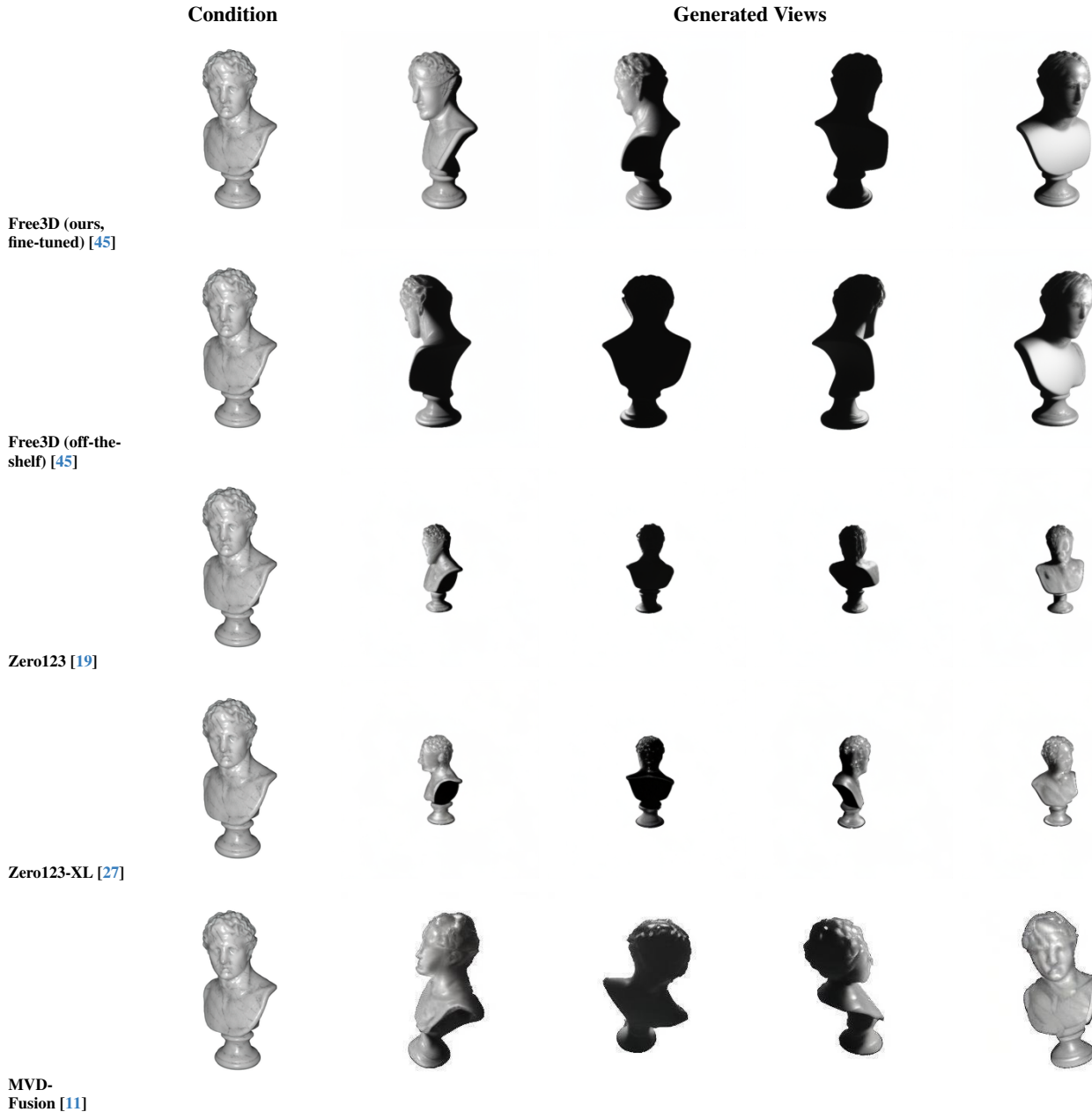


Figure 10. **Multi-view diffusion: comparison on a synthetic “statue” object.** Each row shows novel views generated from a single conditioning image (first column) by different NVS models. Our Free3D fine-tuning better preserves object identity and silhouette coherence than off-the-shelf Free3D and improves geometric consistency over other baselines.

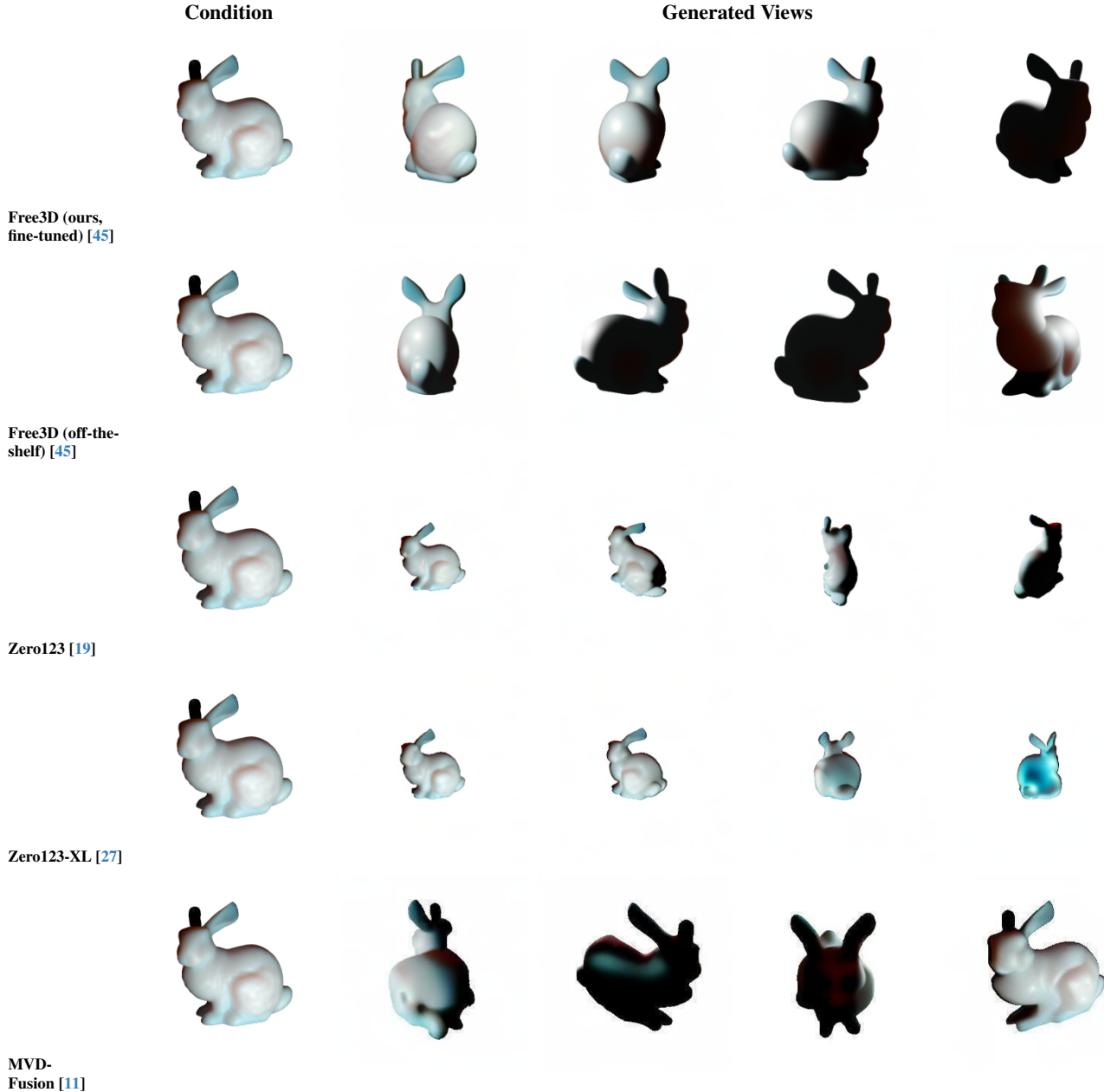


Figure 11. **Multi-view diffusion on a real “bunny” object.** Comparison between our fine-tuned Free3D model and several off-the-shelf NVS baselines. Fine-tuning improves viewpoint coherence and reduces geometric distortions while preserving appearance across views.

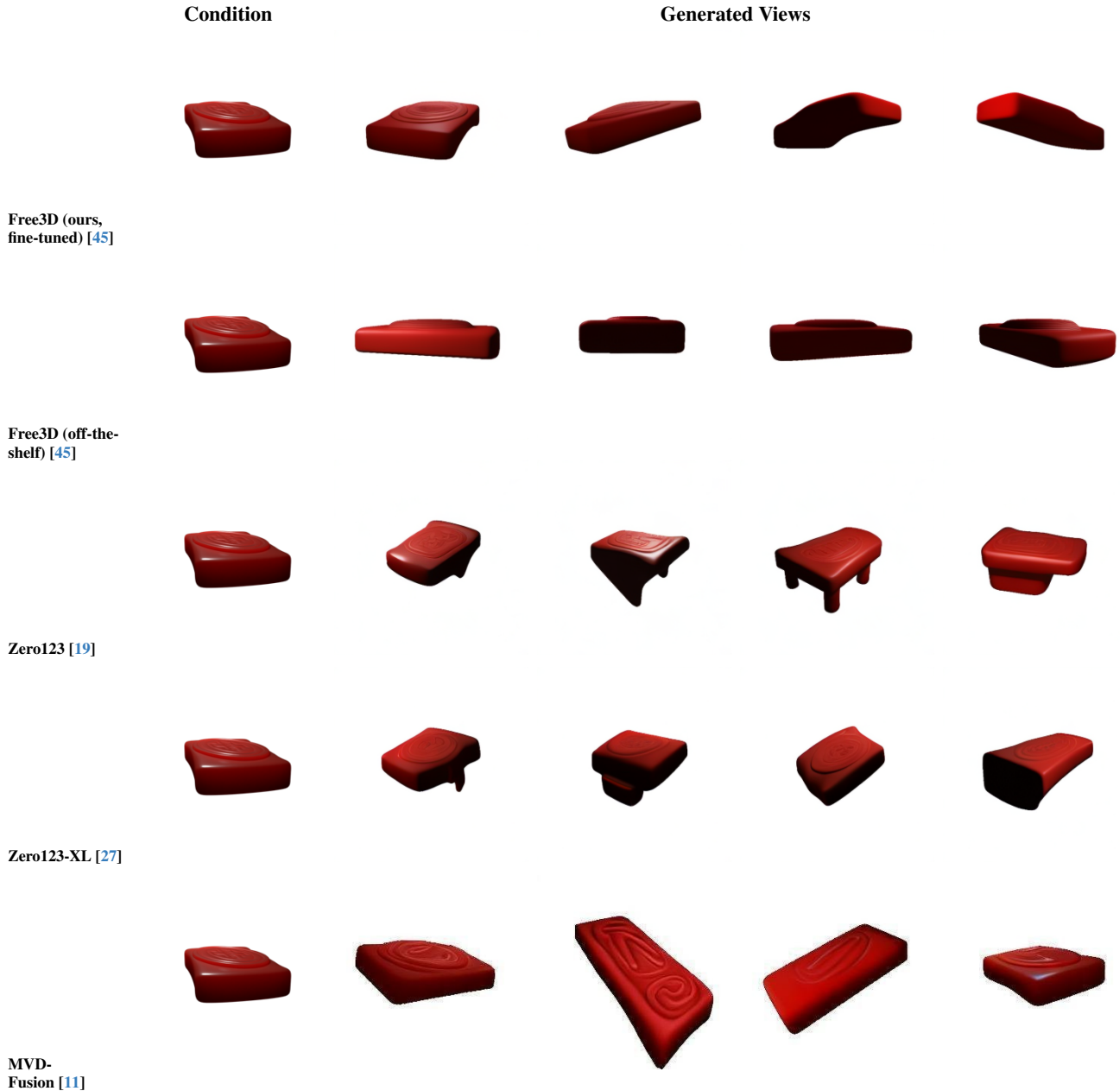


Figure 12. **Multi-view diffusion on a translucent “soap” object.** Our fine-tuned Free3D model better respects the global shape and translucency cues across viewpoints than off-the-shelf Free3D and other NVS baselines, while remaining suitable as an augmentation prior for DIAMOND-SSS.

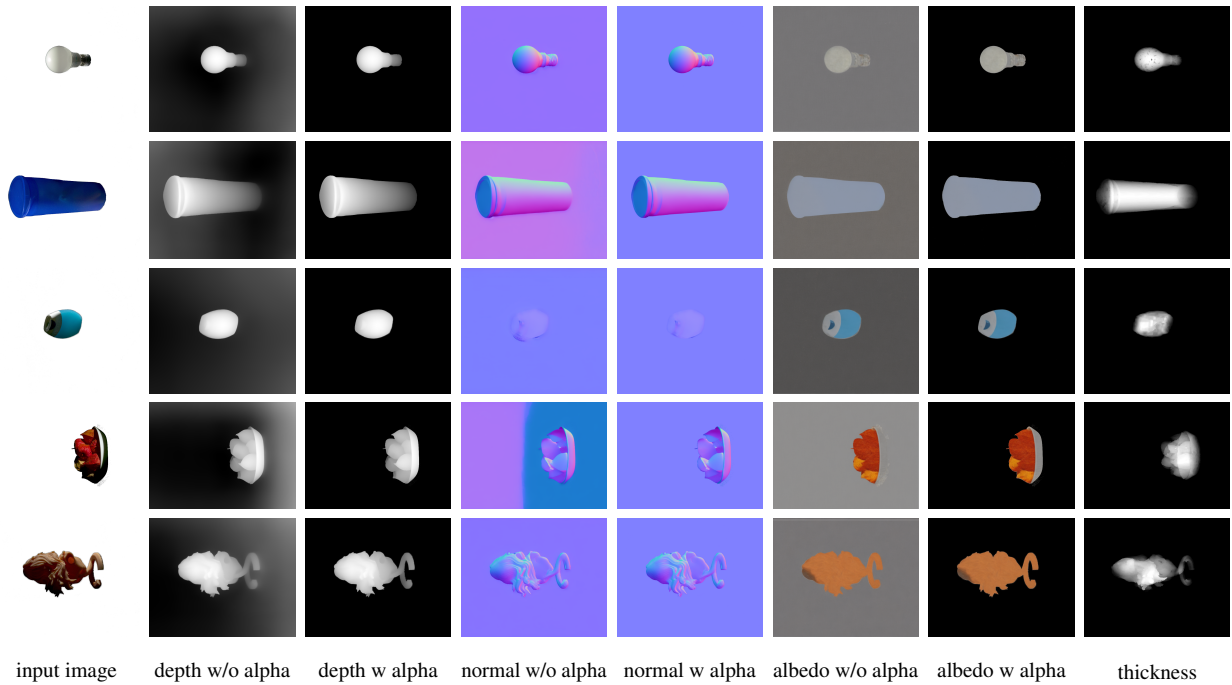


Figure 13. **Samples illustrating the compositing conventions for different conditions.** Each row shows the input RGB image and its corresponding map before and after applying the foreground mask.

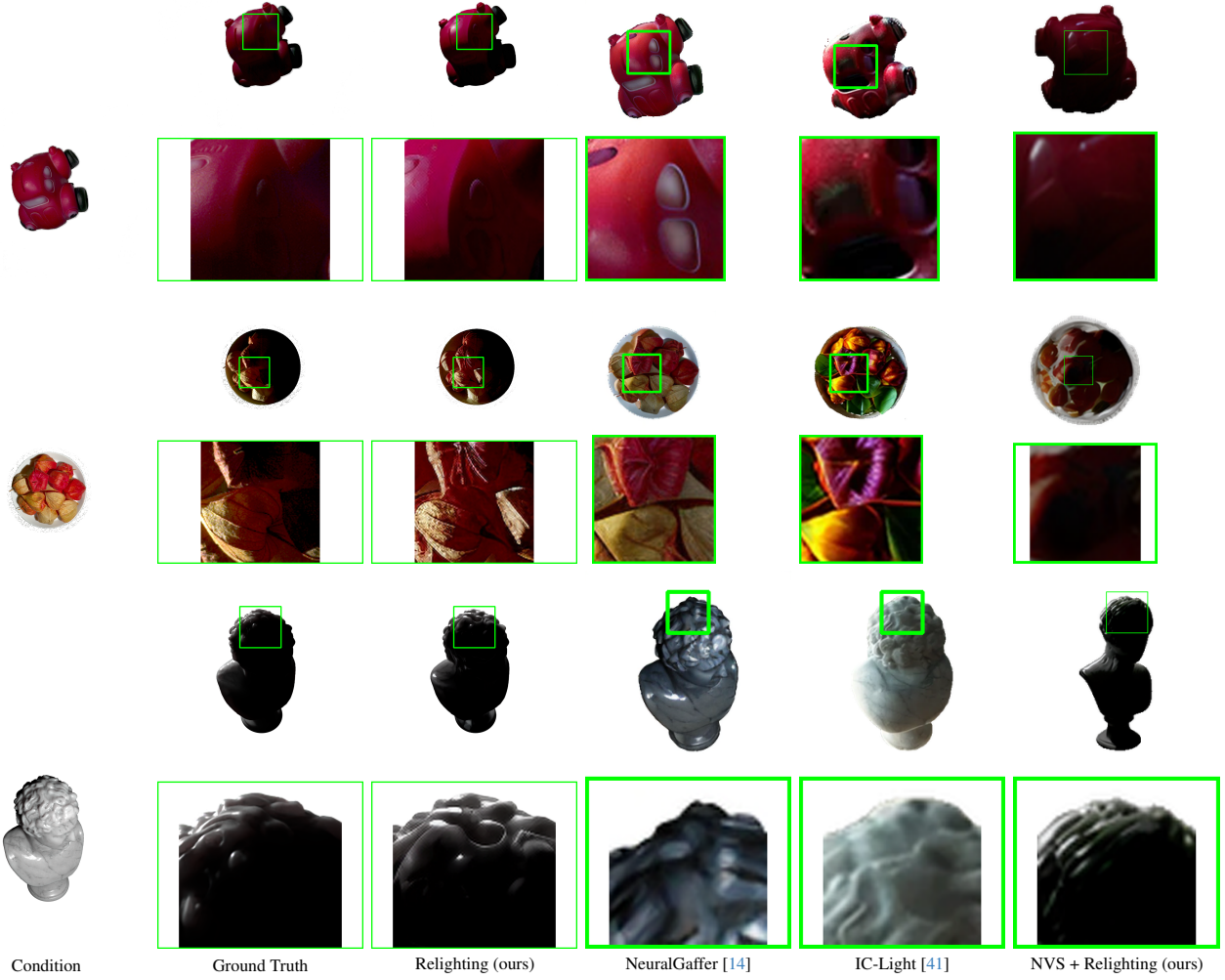


Figure 14. **Qualitative relighting comparison.** For three representative objects (two real, one synthetic), we compare our relighting-only model and our full NVS+relighting pipeline against NeuralGaffer [14] and IC-Light [41] under matched target illumination. Our method better preserves geometry and material appearance, and produces more consistent subsurface scattering cues (e.g., soft shadows and glow) across diverse lighting conditions.

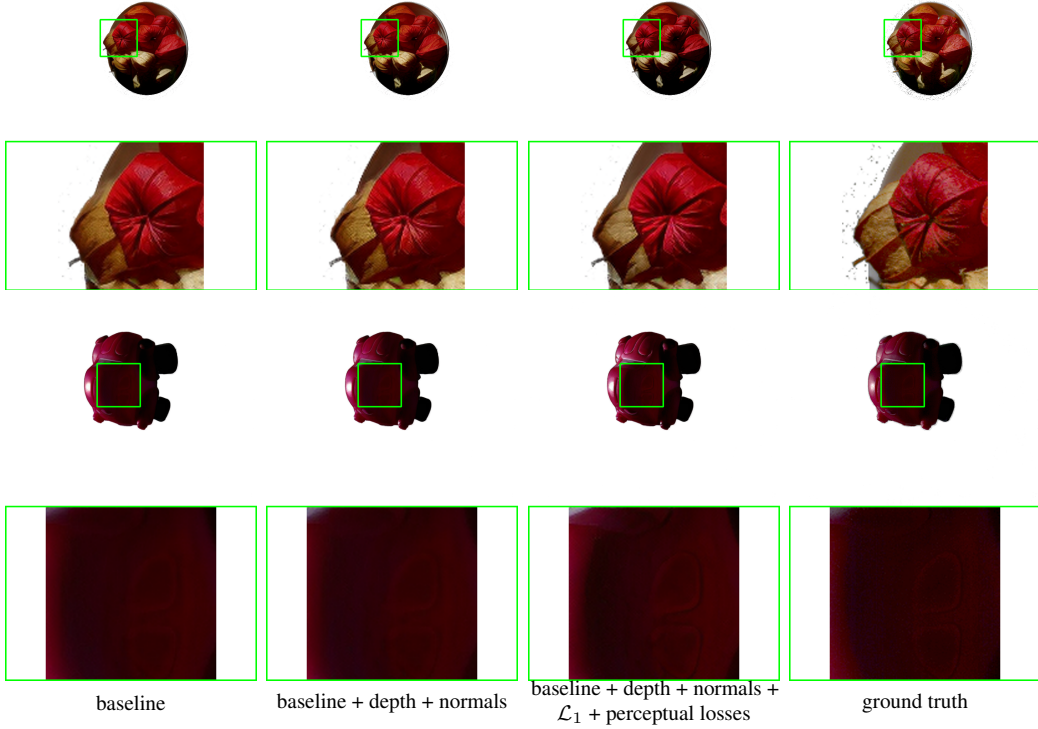


Figure 15. **Relighting ablation.** Effect of progressively adding geometric conditioning (depth, normals) and pixel/perceptual losses to the relighting diffusion model. Additional conditioning and perceptual supervision improve shadow placement, reduce halo artifacts, and better reproduce the soft scattering patterns of translucent materials.

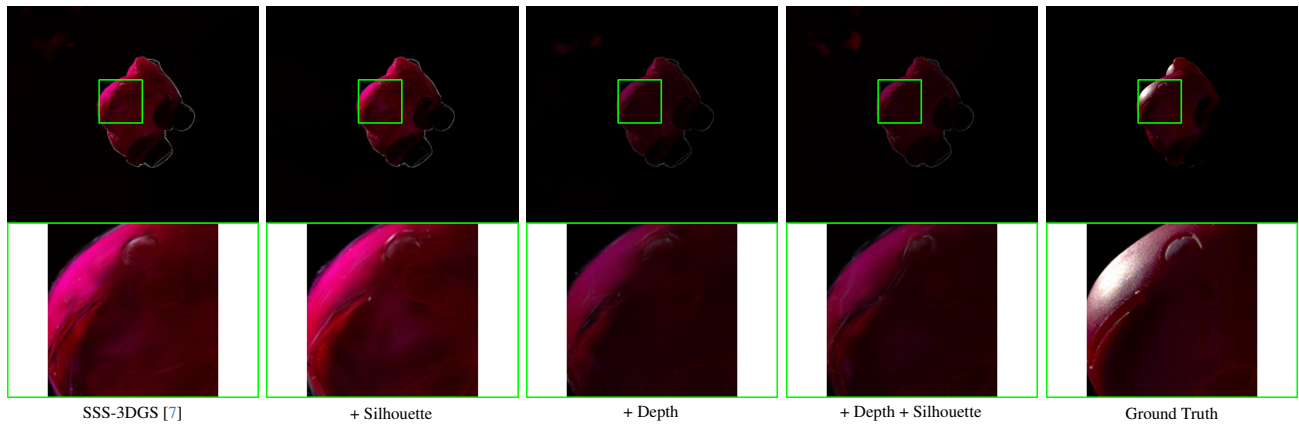


Figure 16. **Synthetic-data ablation of multi-view geometric losses.** Silhouette and depth consistency each improve boundary stability and metric alignment, with the combination yielding the most coherent results.

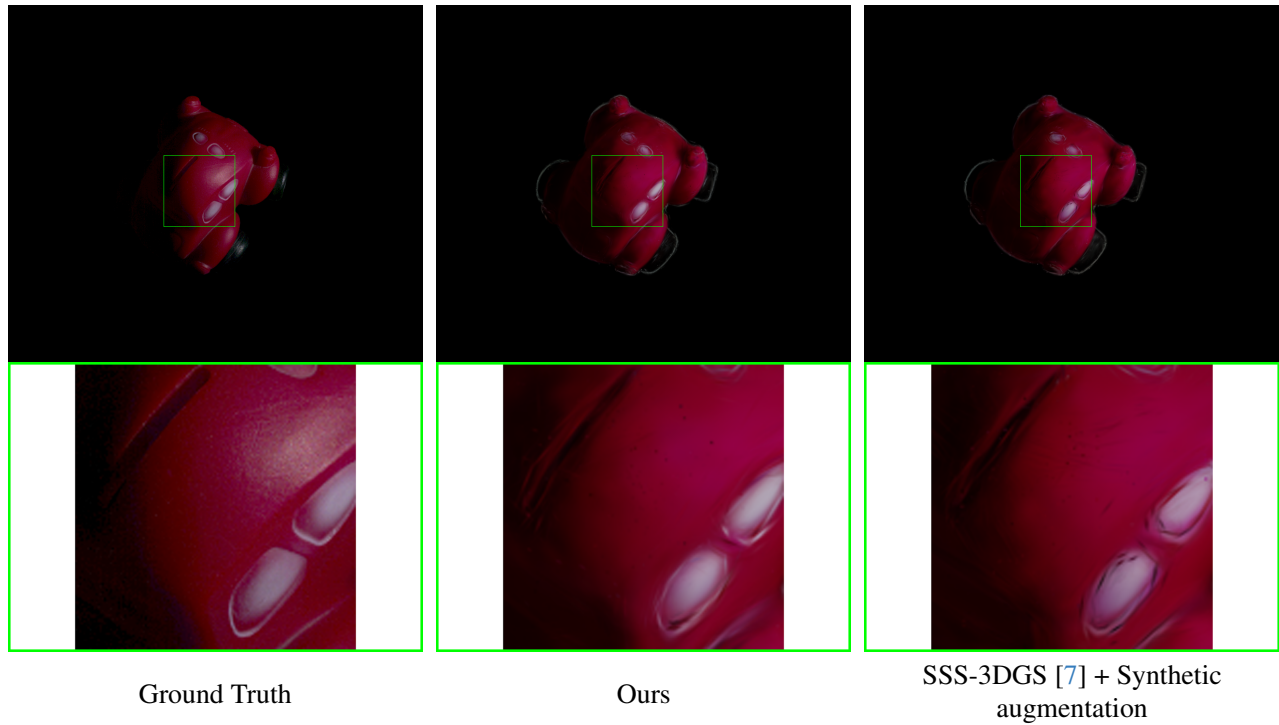
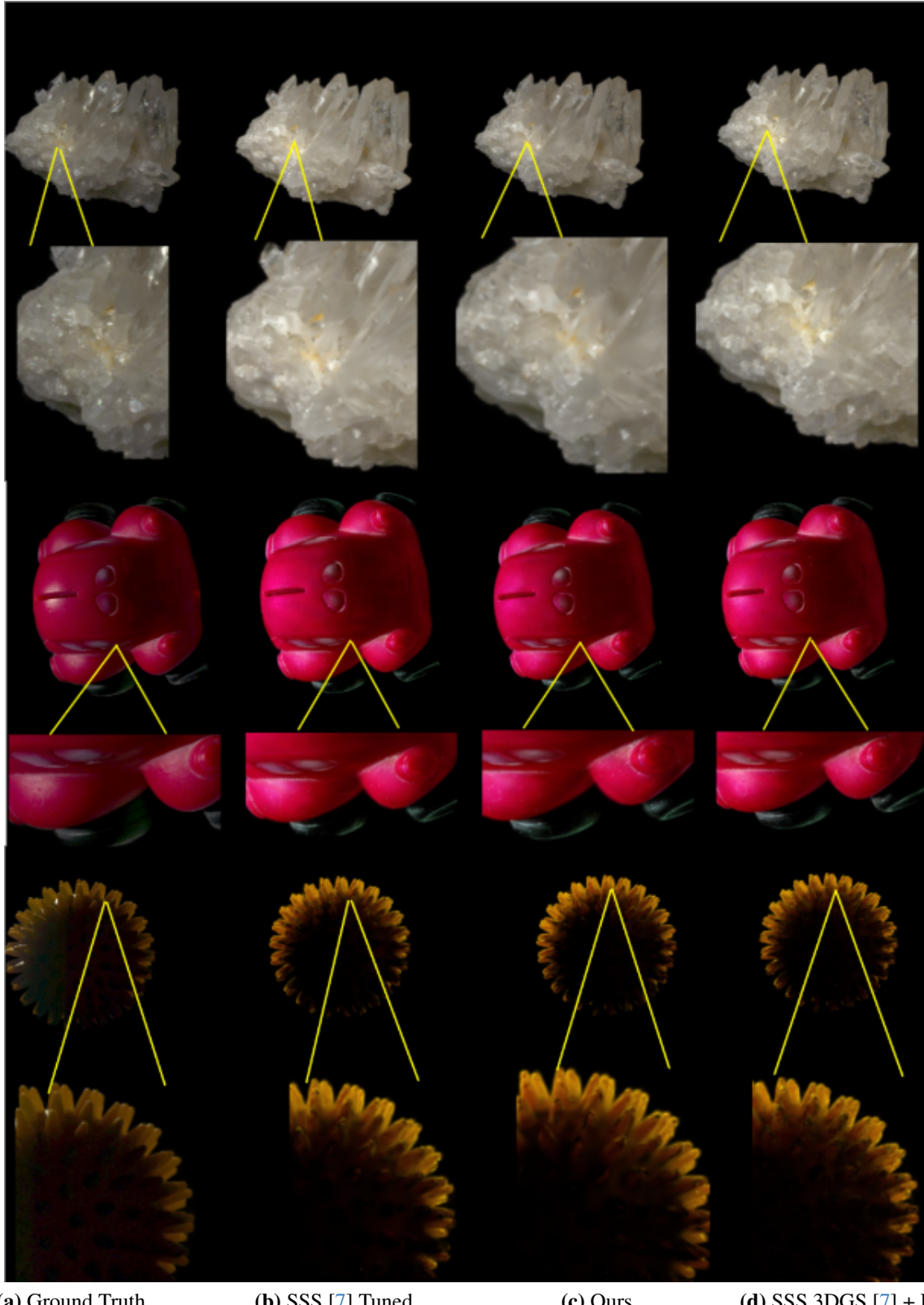


Figure 17. **Real-data reconstruction comparison.** Multi-view geometric losses significantly improve boundary correctness and reduce view-dependent distortions. In this images we are showing the full sampling setting.



(a) Ground Truth

(b) SSS [7] Tuned

(c) Ours

(d) SSS 3DGS [7] + Losses

Figure 18. **Multi-view geometric losses on real objects.** The full multi-view supervision produces sharper boundaries and reduces positional drift. Here we also compare the original method with our tuned hyperparameters.

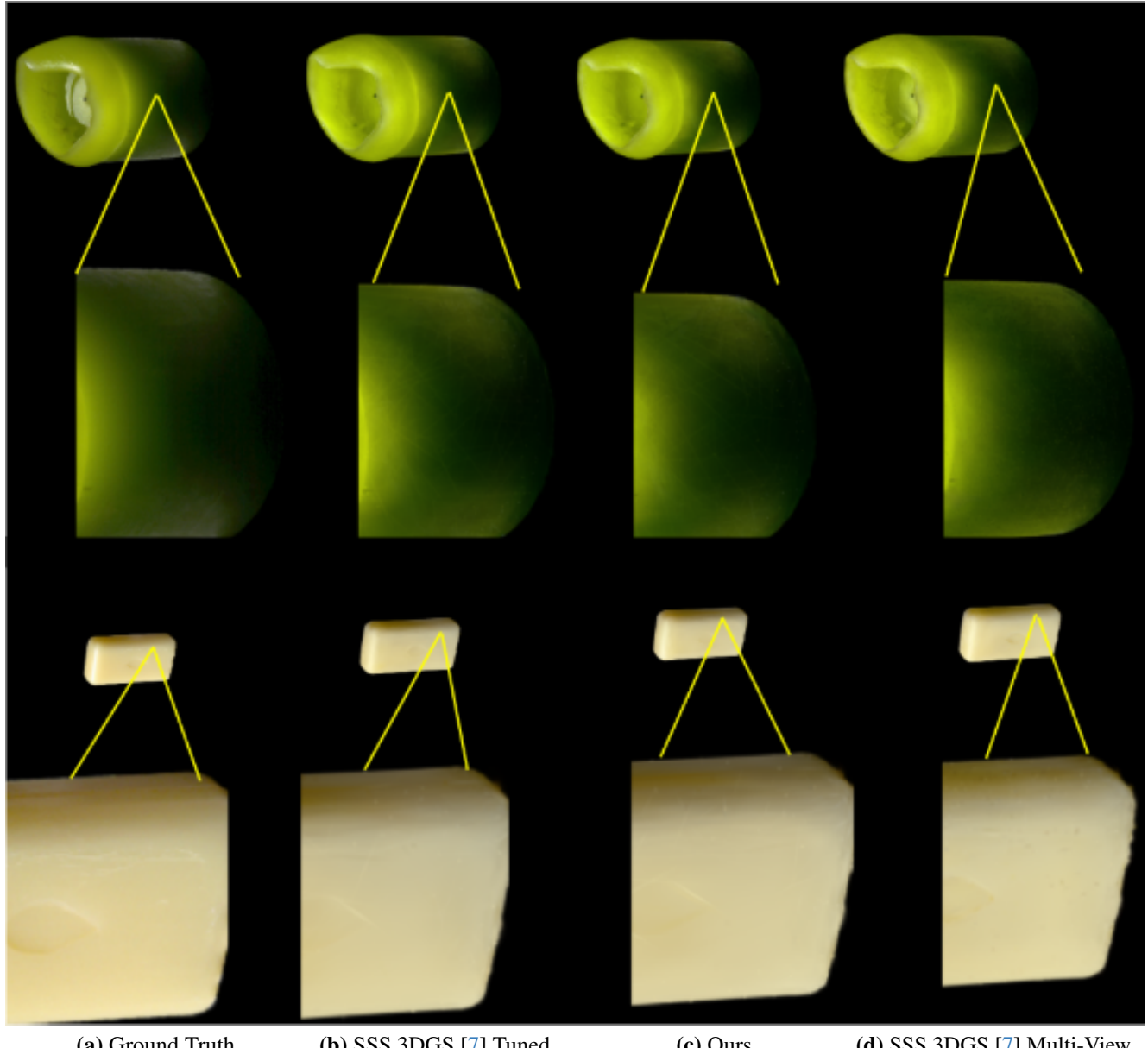


Figure 19. **Synthetic vs. tuned multi-view results.** Combining parameter tuning with multi-view losses yields the most stable reconstructions. Here we also compare the original method with our tuned hyperparameters.

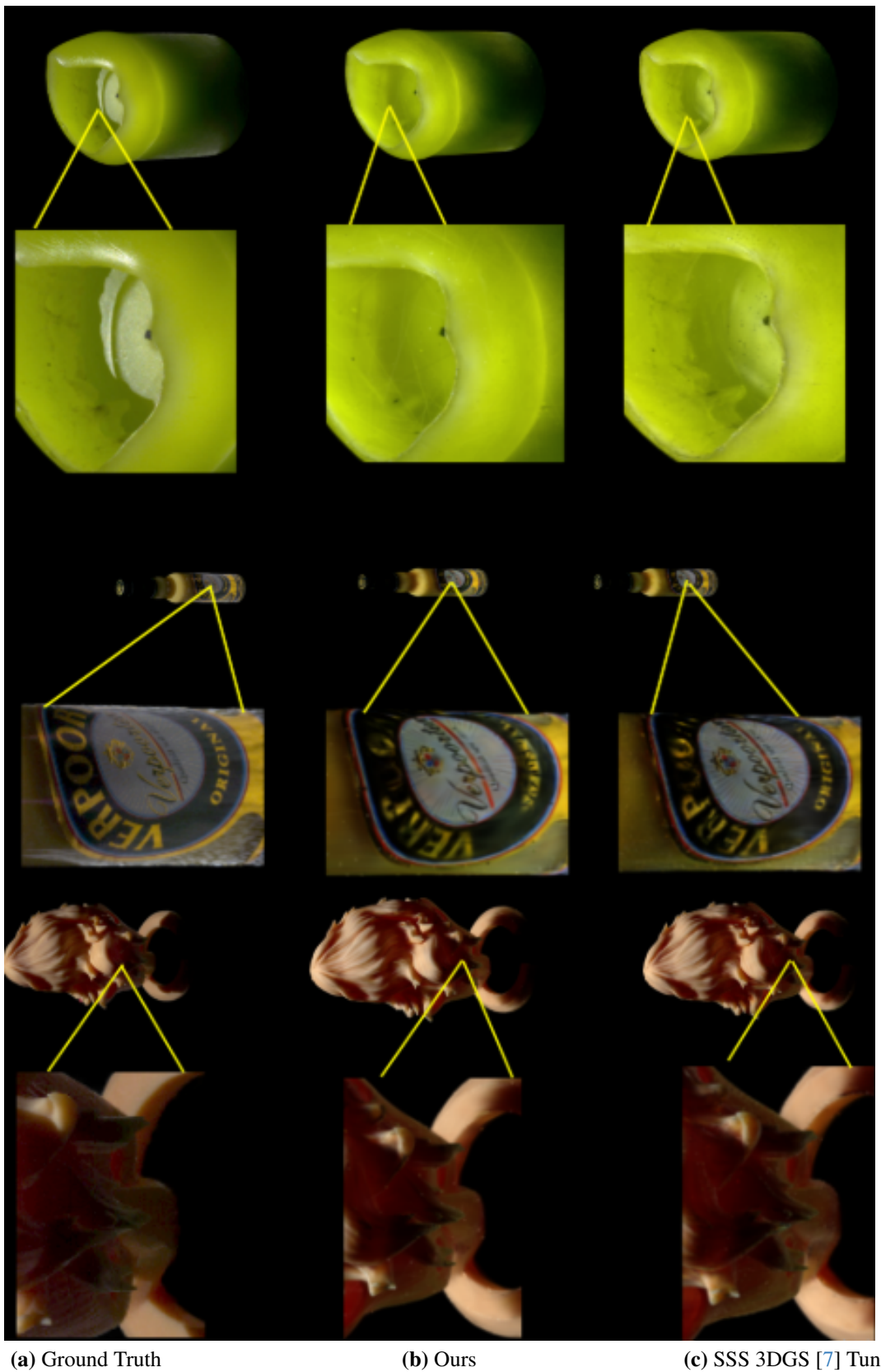
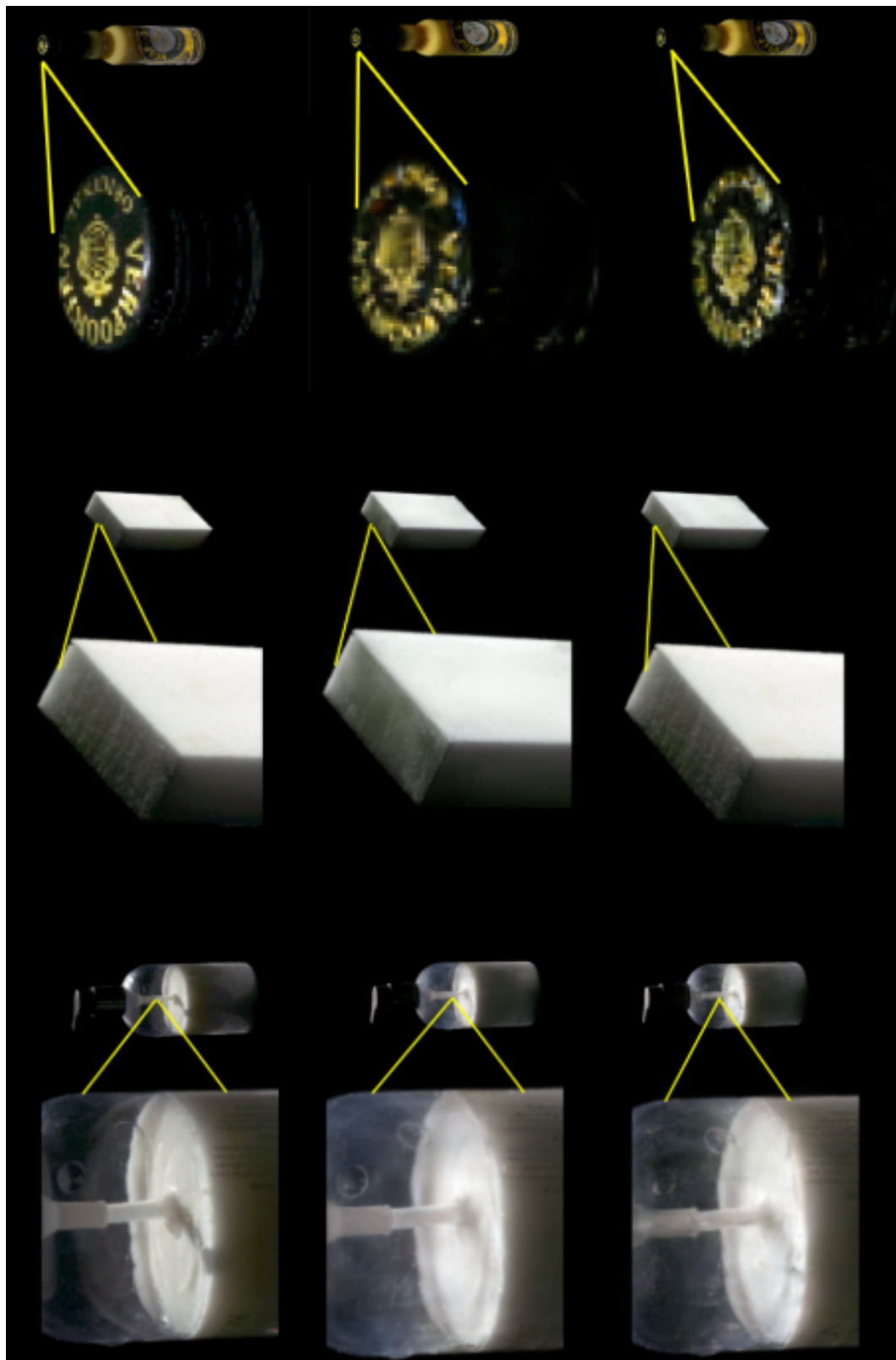


Figure 20. **Silhouette loss effect on synthetic data.** The addition of silhouette regularization reduces boundary bleeding and sharpens object contours.



(a) Ground Truth

(b) Ours

(c) SSS 3DGS [7]

Figure 21. **Silhouette loss effect on synthetic data.** The addition of silhouette regularization reduces boundary bleeding and sharpens object contours.